



저작자표시-비영리-변경금지 2.0 대한민국

이용자는 아래의 조건을 따르는 경우에 한하여 자유롭게

- 이 저작물을 복제, 배포, 전송, 전시, 공연 및 방송할 수 있습니다.

다음과 같은 조건을 따라야 합니다:



저작자표시. 귀하는 원저작자를 표시하여야 합니다.



비영리. 귀하는 이 저작물을 영리 목적으로 이용할 수 없습니다.



변경금지. 귀하는 이 저작물을 개작, 변형 또는 가공할 수 없습니다.

- 귀하는, 이 저작물의 재이용이나 배포의 경우, 이 저작물에 적용된 이용허락조건을 명확하게 나타내어야 합니다.
- 저작권자로부터 별도의 허가를 받으면 이러한 조건들은 적용되지 않습니다.

저작권법에 따른 이용자의 권리는 위의 내용에 의하여 영향을 받지 않습니다.

이것은 [이용허락규약\(Legal Code\)](#)을 이해하기 쉽게 요약한 것입니다.

[Disclaimer](#)

공학박사학위논문

**A study on phase transformation and deformation
behaviors considering transformation plasticity in steels**

변태 소성을 고려한 철강 소재의

상변태와 변형에 관한 연구

2016년 2월

서울대학교 대학원

재료공학부

김 동 완

ABSTRACT

The recent trends in the automotive industry have mainly focused on increasing the crashworthiness properties of automobiles and at the same time decreasing the fuel consumption and gas emissions. In this point of view, Advanced High Strength Steel (AHSS) offers an opportunity for the development of cost effective and light weight parts with improved safety and optimized environmental performance for automotive applications. Starter of AHSS, for example dual phase (DP) and transformation induced plasticity (TRIP) steels, has a higher strength than previous conventional steel. Next stage, Ultra - Advanced High Strength Steel (U-AHSS) is developed. The representative of the U-AHSS is the twinning induced plasticity (TWIP) steels, which has a much strength and elongation. However this steel are yet to be commercialized in use, mainly because of the high level of Mn, which leads to associated processing problems. Thus, X-AHSS steels, with properties of both AHSS and U-AHSS, are now consider as a new option for commercialized steels. Phase transformation behaviors play an important role to decide material properties of the AHSS. Therefore it is necessary to predict accurate phase transformation behaviors using appropriate model. In this paper, there are various attempts in order to predict phase transformation behaviors of AHSS which included complex transformation behaviors.

Firstly, method of dilatometric analysis to analyze the phase transformation behaviors of AHHS with retained austenite was developed. Developed dilatometric analysis method is based on lattice parameter and atomic volume of each phase and additionally consider transformation plasticity and enrich of alloying element. Using the thermodynamic data and equations embedded in the method, it can distinguish the type of BCC structure. Analysis of two specimens which has different Mn, the strong austenite stabilizer, we can verify the accuracy of developed method and find various parameters concerning transformation plasticity and fraction of retained austenite. This method is preferred to obtain the fraction of final fraction of retained austenite very simply and phase transformation kinetics of retained austenite steel.

Secondly, the dissolution and precipitation of Nb, which has been known as strong carbide-forming element, play a key role in controlling phase transformation kinetics of microalloyed steels. In this study, we analyzed both numerically and experimentally the precipitation behavior of Nb-microalloyed steel and its effect on the austenite decomposition during cooling. Nb precipitation in austenite matrix could be predicted by the thermo-kinetic software MatCalc, in which interfacial energy between precipitate and matrix is calculated. The simulated precipitation kinetics were fairly well agreement with the experimental observations by TEM. Austenite decomposition, which is strongly affected by Nb precipitaion during cooling, was measured by

dilatometry and was modeled on the basis of a Johnson–Mehl–Avrami–Kolmogorov (JMAK) equation. It was confirmed that the dissolved Nb delays the austenite decomposition, whereas, the precipitated Nb performs as nucleation sites of phase transformation during the austenite decomposition..

Lastly, a finite element model was developed to predict the deformation, temperature history, carbon diffusion, phase fraction, and hardness during the carburizing heat treatment of automotive annulus gear ring, initially made of a medium carbon steel. Carburizing gas with a constant carbon potential for entire surfaces of the gear was assumed. The temperature and pressure driven carbon diffusion was solved by the finite element simulation based on Fick’s law. Both the diffusional and displacive phase transformations during the heat treatment were modeled incorporating the carbon concentration inside the gear. The constitutive equation of the transformation plasticity was incorporated into the finite element model. Strains due to the phase transformation, transformation plasticity, and thermal expansion/contraction were calculated by the finite element model. The prediction accuracy for the phase evolution, hardness distribution, and dimensional change of the gear ring was verified with the measurement data.

From this study, phase transformation model in X-AHSS, which has not been clear up to now, is described well. The developed model and suggested analysis method lead to a clearer understanding about phase transformation behaviors and related phenomenon of ferrous alloys. Furthermore, using

developed model coupled with finite element simulation or material property prediction model, we can predict the changes of microstructural characteristics and thermal-mechanical behaviors during complex phase transformation.

Keywords: Advanced High Strength Steel (AHSS), Thermo-mechanical modeling, Dilatometric analysis, Transformation plasticity, Precipitation, Matcalc, Carburizing, Finite Element Method (FEM), Hardness, Phase transformation

Student number: 2010-20577

Contents

Abstract	I
Table of Contents	V
List of Tables	IX
List of Figures	XI

Chapter 1

Introduction

1.1 Advanced high strength steel	
	1
1.2 Phase transformation model	3
1.3 Transformation plasticity	5
1.4 Motivation of the thesis.....	7
1.5 References	8

Chapter 2

The new dilatometric analysis method for Advanced High Strength Steels with retained austenite

2.1 Introduction	11
2.2 Experimental procedure	17
2.3 Model developemnet	21
2.4 Results and discussion	29
2.5 Conclusion	42
2.6 References	43

Chapter 3

A model for phase transformation of microalloyed low carbon steel combined with Nb precipitation kinetics

3.1 Introduction	46
3.2 Experimental procedure	49

3.3 Model developemnet.....	52
3.4 Results and discussion	61
3.5 Conclusion	75
3.6 References	76

Chapter 4

A finite element simulation for carburizing heat treatment of automotive gear ring incorporating transformation plasticity

4.1 Introduction	79
4.2 Experimental procedure	84
4.3 Model developemnet.....	87
4.4 Results and discussion	103
4.5 Conclusion	118

4.6 References	119
-----------------------------	-----

Chapter 5

Total conclusion	125
-------------------------------	-----

LIST OF TABLES

Table 2.1 Chemical composition of AHHS with various Mn content.

Table 2.2 Correction factor of thermal expansion, fraction of each phase, constant of transformation plasticity of each condition.

Table 2.3 Fraction of FCC and BCC phase after cooling process using various method.

Table 3.1 Chemical composition of low-carbon Nb micro-alloyed steel.

Table 3.2 The values of k and n from JMAK equation for various phase transformation.

Table 3.3 Radius and relative phase fraction of precipitates at 865 °C for different soaking times.

Table 4.1 The values of k and n from JMAK equation for various phase transformations.

Table 4.2 Densities of each phases as a function of temperature and chemical composition.

Table 4.3 Elastic modulus, Poisson's ratio and thermal conductivity of steel at various temperatures.

LIST OF FIGURES

Figure 2.1 Map for the combination of tensile strength and elongation of various classes of the high-strength sheet steel as the engineering measure

Figure 2.2 Dilatometric curve of low carbon steel showing length change of specimen after thermal cycle.

Figure 2.3 Analysis of dilatometric result using Lever rule method – (a) conventional steel, and (b) retained austenite steel.

Figure 2.4 Schematic diagram of heat treatment for dilatometric analysis - (a) Heating above a_{e3} temperature and (b) heating between a_{e3} and a_{e1} temperature

Figure 2.5 Flow chart of developed dilatometric analysis method based on lattice structure, transformation plasticity, and carbon enrich.

Figure 2.6 (a) Comparison between experimental data and developed analysis

method concerning temperature and strain graph. (b) Comparison between Lever rule method and developed analysis. (c) Type of transformed BCC phase and (d) optical microstructure after cooling process (Specimen: LMn steel, Holding temperature: 950 °C, Cooling rate: 0.5 °C/sec)

Figure 2.7 (a) Comparison between experimental data and developed analysis method concerning temperature and strain graph. (b) Type of transformed BCC phase and (c) optical microstructure after cooling process (Specimen: LMn steel, Holding temperature: 950 °C, Cooling rate: 20 °C/sec)

Figure 2.8 (a) Comparison between experimental data and developed analysis method concerning temperature and strain graph. (b) Type of transformed BCC phase and (c) optical microstructure after cooling process (Specimen: HMn steel, Holding temperature: 950 °C, Cooling rate: 20 °C/sec)

Figure 2.9 Dilatation result of the steel with various holding temperature - (a) 650 °C, (b) 670 °C, and (c) 690 °C

Figure 2.10 Analyzed phase transformation kinetics during heating process -

(a) 650 °C, (b) 670 °C, and (c) 690 °C

Figure 2.11 Analyzed phase transformation kinetics during cooling process -

(a) 650 °C, (b) 670 °C, and (c) 690 °C

Figure 2.11 EBSD images after cooling process with various holding

temperature- (a) 650 °C, (b) 670 °C, and (c) 690 °C

Figure 3.1 Schematic diagram of heat treatment for TEM observation.

Figure 3.2 Schematic diagram of heat treatment for dilatometric analysis (a)

observing solid solution effect of Nb (b) observing precipitation effect of Nb.

Figure 3.3 TEM image of steel_1 soaked at 865 °C for (a) 10 min, (b) 30 min,

(c) 180 min and (d) 300 min.

Figure 3.4 TEM image of steel_2 soaked at 865 °C for (a) 10 min, (b) 30 min,

(c) 180 min and (d) 300 min.

Figure 3.5 (a) High resolution TEM image, (b) diffraction pattern (c) EDS data of Nb precipitates.

Figure 3.6 Comparison of (a) relative phase fraction and (b) precipitates radius with various conditions.

Figure 3.7 Relative fraction of precipitates concerning the effect of (a) interfacial energy, (b) grain size, and (c) dislocation density.

Figure 3.8 Change of interfacial energy due to change of chemical composition and precipitate radius.

Figure 3.9 (a) Difference of Volume free energy change on nucleation formation and (b) critical nucleation energy due to Si content.

Figure 3.10 (a) Comparison of relative phase fraction and between MatCalc calculation (Line) and TEM observation (Symbol). (b) precipitate-time-temperature graph of Nb-micro alloyed steels.

Figure 3.11 Comparison of relative phase fraction between MatCalc

calculation (Line) and TEM observation (Symbol) considering Nb precipitation effect. (a) steel_1 and (b) steel_2.

Figure 3.12 Change of the phase transformation kinetics due to Si addition.

Figure 4.1 Image of annulus gear ring made of SCR420 steel.

Figure 4.2 Schematic diagrams of carburizing heat treatment. (a) Carburizing at 930 °C and holding at 830 °C – case 1, and (b) carburizing at 800 °C and holding at 750°C – case 2. C.P means carbon potential.

Figure 4.3 Flow chart of the developed finite element model.

Figure 4.4 (a) Heat capacity of each phases and (b) heat evolution due to the phase transformation.

Figure 4.5 (a) Calculated distribution of carbon concentration after carburizing condition in case 1 and (b) calculated (line) and measured (symbol) carbon concentration profiles in case 1 (red) and case 2 (blue).

Figure 4.6 (a) Phase transformation behavior at various cooling rates and microstructure of 0.22 wt% carbon steel under cooling rates of (b) 1 °C/s, (c) 2 °C/s, (d) 10 °C/s, (e) 20 °C/s, and (f) 40 °C/s.

Figure 4.7 (a) Phase transformation behavior at various cooling rates and microstructure of 0.51 wt% carbon steel under cooling rates of (b) 1 °C/s, (c) 2 °C/s, (d) 10 °C/s, (e) 20 °C/s, and (f) 40 °C/s.

Figure 4.8 Phase diagram of 0.26 wt%Si-0.85 wt%Mn-1.26 wt%Cr steel as a function of carbon under para-equilibrium.

Figure 4.9 Microstructure of the gear ring after the carburizing heat treatment (a) at the gear surface in case 1, (b) at the gear inside in case 1, (c) at the gear surface in case 2, and (d) at the gear inside in case 2.

Figure 4.10 Measured (flat bar) and calculated (diagonal lined bar) phase fraction of ferrite (red) and martensite (green) phase after the carburizing heat treatment (a) at the gear surface in case 1, (b) at the gear inside in case 1, (c)

at the gear surface in case 2, and (d) at the gear inside in case 2.

Figure 4.11 Radial length change of the annulus gear during the carburizing heat treatment with transformation plasticity (red line) and without transformation plasticity (black line).

Figure 4.12 Comparisons between the calculated length change with transformation plasticity (red bar), without transformation plasticity (blue bar), and measured length change (black bar) carburized by carburizing heat treatment in (a) case 1 and (b) case 2.

Figure 4.13 Comparisons between the measured (line) and calculated (symbol) profiles of hardness after carburizing heat treatment in case 1 (red) and case 2 (blue).

Chapter 1

Introduction

1.1 Advanced high strength steel

The recent trends in the automotive industry have mainly focused on increasing the crashworthiness properties of automobiles and at the same time decreasing the fuel consumption and gas emissions. In this point of view, Advanced High Strength Steel (AHSS) offers an opportunity for the development of cost effective and light weight parts with improved safety and optimized environmental performance for automotive applications [1-5]. Starter of AHSS, for example dual phase (DP) and transformation induced plasticity (TRIP) steels, has a higher strength than previous conventional steel. Next stage, Ultra - Advanced High Strength Steel (U-AHSS) is developed. The representative of the U-AHSS is the twinning induced plasticity (TWIP) steels, which has a much strength and elongation. However this steel are yet to be commercialized in use, mainly because of the high level of Mn [6,7], which leads to associated processing problems. Thus, X-AHSS steels, with properties of both AHSS and U-AHSS, are now consider as a new option for commercialized steels.

Both TRIP and TWIP steels are complex microstructures containing

retained austenite added to increase strength and enhance strain hardening. The X-AHSS is also basically an adaptation of these microstructures with a significant amount of metastable austenite above TRIP levels [9-11].

1.2 Phase transformation model

The transformed phase fraction, X , during isothermal austenite decomposition has been characterized using the JMAK type equation [12] as follows:

$$X = X^e \left[1 - \exp(-kt^n) \right] \quad (1)$$

where X^e is the thermodynamic equilibrium fraction, which can be determined from the equilibrium phase diagram at a given chemical composition and temperature, t is the total time for transformation. The rate constant k depends on the temperature, chemical composition, austenite grain size and precipitation behaviors. The time exponent n is a constant over the temperature range when a chemical composition of steel is determined.

In order to extend the JMAK equation for phase transformation to the nonisothermal condition, the concept of additivity rule [13], which is based on the theory of Scheil [14], was introduced under the assumption that the cooling curve can be divided into small time intervals within which the kinetics values remain constant. The transformed phase fraction until the i th step, X_i , is expressed as follows:

$$X_i = X_i^e \{1 - \exp[-k_i(t' + \Delta t)^n]\} \quad (2)$$

$$t' = \left[-\frac{1}{k_i} \ln \left(\frac{1 - X_{i-1}}{X_i^e} \right) \right]^{1/n} \quad (3)$$

where t' is equivalent transformation time needed to transform into the fraction of X_{i-1} at the temperature of the i th step, and Δt is the time step corresponding to the i th step. The values, k and n were determined from the dilatation data obtained by the continuous cooling tests using an inverse additivity technique. The k and n values of the austenite to ferrite, widmanstatten ferrite, pearlite and bainite transformations are made of function of chemical composition, austenite grain size and temperature.

1.3 Transformation plasticity

The transformation plasticity refers to the permanent deformation that occurs when the phase transformation of ferrous or other alloys progresses under an applied stress, which is even much lower than the yield stress of the material. The description for the transformation plasticity can be classified into three main groups according to their mechanisms: (1) the weaker phase yielding [15], (2) the favorable variant selection [16,17], and (3) the accelerated diffusion on the migrating transformation interface [18]. First of these mechanisms explains the macroscopic plasticity induced by the volume mismatch between hard and soft phases, which produces the microscopic plasticity in the weaker phase. Several researchers proposed several modified models based on empirical evidences such as the proportionality of the permanent strain to the applied stress and the difference of lattice volumes between the two phases [19,20]. Second important mechanism accounts the anisotropy of the transformation strain during the displacive transformation [16,21,22]. Some of the authors modeled the anisotropic transformation strain based on the selectivity of some specific variants increased by the externally applied stress during the displacive transformation. Another microstructural theory for transformation strain is based on the diffusion mechanism of the migrating interface during the diffusional phase transformation, which can be

described as an accelerated Coble creep [18]. Some of the authors derived a constitutive equation for the transformation plasticity as a thermally activated form by considering an atomic flux along the phase interface.

1.4 Motivation of the thesis

Phase transformation behaviors play an important role in improving material properties of steels. Therefore it is necessary to predict accurate phase transformation behaviors using appropriate model. However, classical phase transformation model is mostly based on only the effect of alloying element and temperature, and this causes a certain limitation to predict phase transformation behaviors of complex AHSS, for which retained austenite, precipitation, and carburizing should be considered. Therefore, in this paper there are various attempts to overcome those limitations. Concretely, in order to analyze the amount and transformation kinetic of retained austenite, we propose a new dilatometric analysis method based on lattice structure and lattice parameter. We also solve the precipitation nucleation equation and mass diffusion equation, then and couple them in a for phase transformation model to incorporate the effect of the precipitation and carburizing on phase transformation.

1.5 References

- [1] H. Aydin, E. Essadiqi, I.-H. Jung, S. Yue. Mater. Sci. Eng. A 564 501-508 (2013)
- [2] H.N. Han, C.-S. Oh, G. Kim, O. Kwon, Mater. Sci. Eng. A 499 462-468 (2009)
- [3] R.H.Wagoner, Report: Advanced High-Strength Steel Workshop, Arlington, Virginiaia, USA, October 22–23, 2006.
- [4] D.K. Matlock, J.G. Speer, Proceedings of the Third International Conference on advanced Structural Steels, 2006, pp. 774–781.
- [5] O. Kwon, S.-K. Kim, G. Kim, Proceedings of the 21st Conference on Mechanical Behaviors of Materials, Changwon, Korea, October 18–19, 2007.
- [6] H.K.D.H. Bhadeshia, R.W.K. Honeycombe, Steels: Microstructure and Properties, Elsevier, Butter worth–Heinemann, Amsterdam, Boston, 2006
- [7] S.Keeler (Ed.), in: Proceedings of the Advanced High Strength Steel (AHSS) Application Guidelines, 2009.
- [8] Y. Weng, H. Dong, Y.X. Gan, Springer, Metallurgical Industry Press, Berlin, Heidelberg, NewYork, 2011S. 1.

- [9] D.K. Matlock, J.G. Speer, Third generation of AHSS: microstructure design concepts, in: A. Haldar, S. Suwas, D. Bhattacharjee(Eds.), Proceedings of the International Conference on Microstructure and Texture in Steels, Springer, London, 2009, pp.185–205.
- [10] H. Aydin, H.K. Zeytin, H. Cimenoglu, Effect of micro alloying elements and deformation mechanisms on the twip steels, in :S.M. Howard(Ed.), Epd Congress 2009, Proceedings, 2009, pp.191–197.
- [11] E. De Moor, J.G. Speer, D.K. Matlock, J.-H. Kwak, S.-B. Lee, Steel Res. Int. 83 322–327 (2012)
- [12] W.A. Johnson, R.F. Mehl, Trans. AIME. 135 416 (1937)
- [13] H.N. Han, J.K. Lee, ISIJ Int. 42 200-205 (2002)
- [14] E. Sheil, Archiv fuer Eisenhuettenwesen 8 (1935) 565.
- [15] G.W. Greenwood, R.H. Johnson, The deformation of metals under small stresses during phase transformations, Proc. R. Soc. A. (London) 83 403 (1965)
- [16] H.N. Han, C.G. Lee, C.-S. Oh, T.-H. Lee, S.-J. Kim, Acta Mater. 52 5203-5214 (2004)
- [17] M.-G. Lee, S.-J. Kim, H.N. Han, Int. J. Plast. 26 688-710 (2010)
- [18] H.N. Han, J.K. Lee, D.-W. Suh, S.-J. Kim, Philos. Mag. 87 159-176 (2007)

- [19] Y. Desalos, Comportement dilatométrique et mécanique de l'Austénite Métastable d'un Acier A 533, IRSID Report n. 34 (1981) 44.
- [20] P. Zwigl, D.C. Dunand, Mater. Sci. Eng. A 262 166-172 (1999)
- [21] H.N. Han, D.-W. Suh, Acta Mater. 51 4907-4917 (2003)
- [22] H.N. Han, C.-S. Oh, G. Kim, O. Kwon, Mater. Sci. Eng. A 499 462-468 (2009)

Chapter 2

The new dilatometric analysis method for Advanced High Strength Steels with retained austenite

2.1 Introduction

In steel technology, many attempts of improvements were made to make vehicles with reduced weight and increased safety, and those improvements have been recently undertaken to develop more efficient steel that are micro alloyed. In this point of view, Advanced High Strength Steel (AHSS) offers an opportunity for the development of cost effective and light weight parts with improved safety and optimized environmental performance for automotive applications [1-5]. Starter of AHSS, for example dual phase (DP) and transformation induced plasticity (TRIP) steels, has a higher strength than previous conventional steel. Next stage, Ultra - Advanced High Strength Steel (U-AHSS) is developed. The representative of the U-AHSS is the twinning induced plasticity (TWIP) steels, which has a much strength and elongation. However this steel are yet to be commercialized in use, mainly because of the high level of Mn [6,7], which leads to associated processing problems. Thus, X-AHSS steels, with properties of both AHSS and U-AHSS,

are now consider as a new option for commercialized steels, as shown at Fig.1 [8].

Both TRIP and TWIP steels has the complex microstructures that contain retained austenite to increase strength and elongation. The X-AHSS also has these microstructures such as metastable austenite above TRIP levels [9-11]. Therefore it is very important to measure transformation kinetics as well as final fraction of retained austenite, and various experimental method such as optical microscope (OM), scanning electron microscope (SEM), electron backscatter diffraction (EBSD) have been employed for measurements [12]. However, determining fraction of retained austenite using above mentioned methods faces a limitations since they require too many experimental procedures and time, and they can only be carried out for the final microstructure of the specimen. Furthermore, this leads to a limitation of obtained transformation kinetics of retained austenite as well. The dilatometric analysis on the other hand, was found to be suitable for obtaining kinetics of phase transformation, and was used over the last few decades for the study of solid state phase transformations in ferrous alloys [13-15]. When a solid state phase transformation occurs, the dilatation curve provides information on the resulting atomic volume change, as well as the thermal expansion of the specimen. Conventionally, the volume fraction of the individual phases in the specimen is determined by the application of a lever

rule to the dilatation curve. This method starts with the extrapolation of the two linear segments corresponding to the parent and transformed phases on the dilatation curve, respectively. As shown at Fig. 2a, the fraction of the transformed phase at a given temperature, in the lever rule, can be evaluated from the relative position between the two extrapolated linear lines of the dilatation curve. However, unfortunately, as shown at fig 2b, if the steel has a retained austenite fraction at room temperature, it is difficult to find the finish point of the phase transformation and make extrapolation line of the two section. In order to overcome this problem with classical Lever rule method, new analysis method is recommend. Austenite has the distinct lattice structure of face centered cube (FCC) as opposed to its decomposed products whose lattices are based on body centered cube (BCC) [13,17]. Because those lattice structures and lattice parameters are well known as function of temperature and alloying element, using this parameters allow us to reconstruct theoretical strain lines if retained austenite exist in steels or not.

All of these new methods were established under the important assumption that the isotropic volume change occurs during the phase transformation. In general, however, it is well known that nonisotropic volume changes in dilatometry are observed during the phase transformation in steel. Fig. 3 shows the dilatometric curve of low-carbon steel undergoing a thermal cycle consisting of continuous heating and cooling. The change of

specimen length would not be found after the thermal cycle if the volume change associated with the phase transformation are isotropic. But the permanent strain appearing in dilatometric curve indicates that the specimen length is changed by the thermal cycle, which implies that the volume change with the transformation has non-isotropic characteristics [13,16,17]. The main reason of this phenomenon is called transformation plasticity (TP), and it is very important to distinguish these permanent strain caused by TP effect and formation of retained austenite [18-21].

In this study, phase transformation kinetics and related phenomenon are analyzed using the developed dilatometric analysis method based on lattice parameters and structures. Parameters related to transformation plasticity were obtained by conducting various cooling and holding experiments. Using this data, we can distinguish the strains due to retained austenite and transformation plasticity, which then allow us to analyze the phase transformation kinetics and final fraction of retained austenite using only the dilatometric analysis.

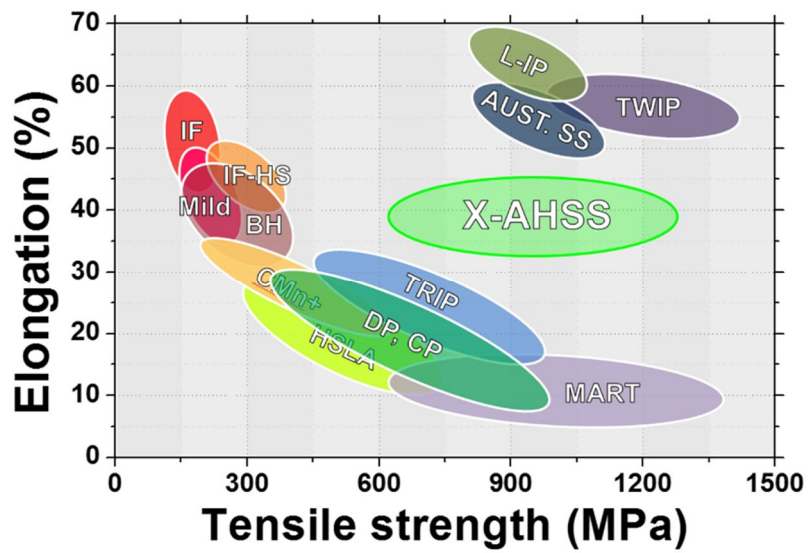


Figure 1.

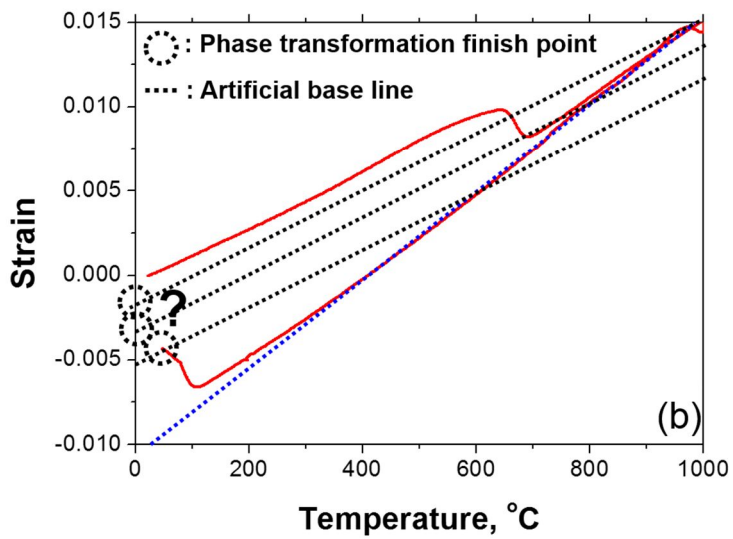
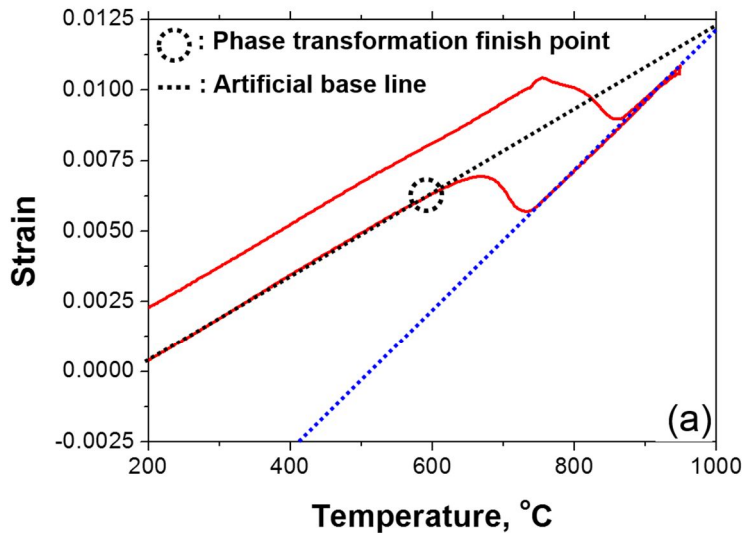


Figure 2

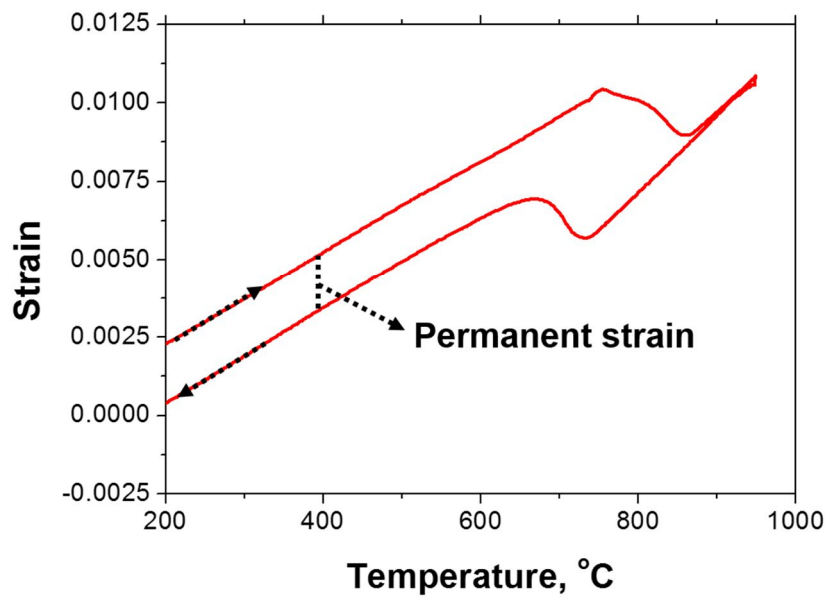


Figure 3

2.2 Experimental procedure

The chemical composition of the advanced high strength steel studied is presented in Table 1. These steels were melted by a high-frequency vacuum induction furnace and were cast into a metallic mold. The 100 mm ingot was homogenized in a protective atmosphere at 1200 °C for 1 hour and hot rolled into a plate of about 6 mm thick.

For the microstructural analysis, an EBSD equipped with FE-SEM (SEM: JSM6500F and EBSD: Oxford Inca System) was used. The samples were prepared by the standard metallographic grinding procedure followed by chemical etching with a solution of 3% nitric acid–97% ethyl alcohol solution and electropolishing with a solution of 20% perchloric acid–80% ethanol for the OM and EBSD measurement, respectively.

To evaluate the phase transformation behaviors, we used the dilatometric measurement performed using a transformation dilatometer (R&B, TM-111129-001). As shown at Fig. 4a, the specimens were heated by an induction coil in a vacuum to 950 °C at a heating rate of 10 °C/s, then austenitized for 10 min, followed by cooling to room temperature at various cooling rates of 0.5 and 20 °C/s. Another condition was represented at Fig. 4b. The specimens were heated to various temperature, 650, 670, 690 °C, between a_{e1} and a_{e3} temperature. In this condition, heating rate is 1 °C/s, austenitizing time is just for 1 min, cooling rates is 20 °C/s.

Table 1.

	C	Si	Mn	S	Cr	N	Al
LMn_steel	0.1	0.1	1.7	0.003	0.1	0.003	0.05
HMn_steel	0.2	1.5	10	0.003	0.1	0.003	0.05

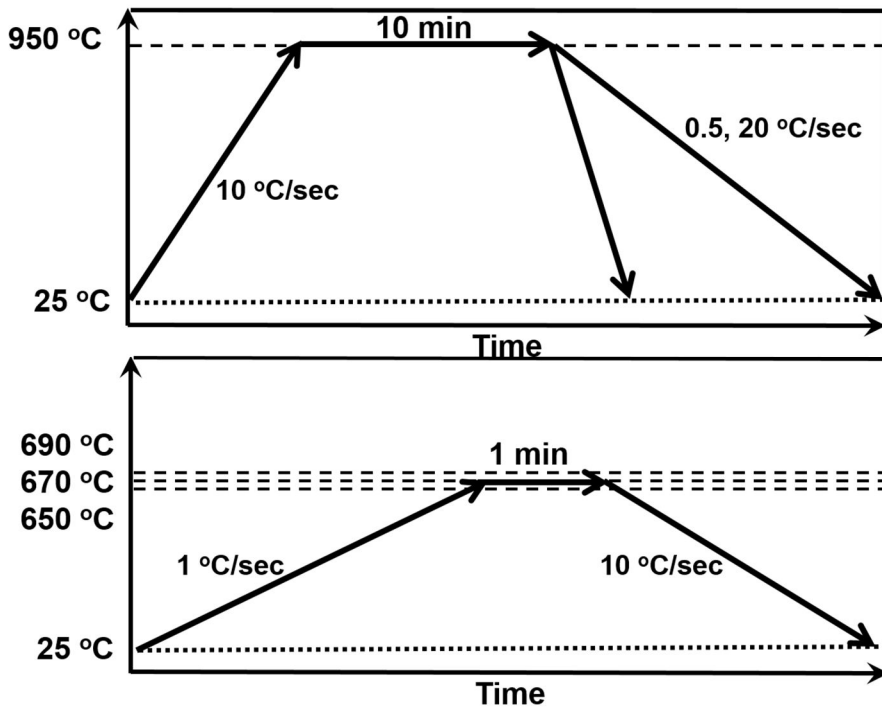


Figure 4

2.3 Model development

2.3.1 Lattice parameter based on dilatometric analysis model

The relative volume change of a specimen can be calculated using the value of the relative length change. When the expansion-contraction of a sample is assumed to be isotropic, equation for the current unit volume is listed below:

$$V = V_0 \left[\left(\frac{\Delta L}{L_0} \right) + 1 \right]^3 \quad (1)$$

where ΔL , L_0 , V , and V_0 , are the length change of the specimen, initial length of the specimen at room temperature, current unit volume, and initial atomic volume, respectively. V can be represented by a sum of atomic volumes of the constituent phases shown below:

$$V = \sum f_i V_i \quad (2)$$

where V_i is the atomic volume and f_i is the fraction of volume at phase i, such as austenite, ferrite and pearlite, respectively. The average atomic volumes of each phases are represented with consideration of the lattice parameter and structure below:

$$V_\alpha = \frac{a_\alpha^3}{4}, \quad V_\gamma = \frac{a_\gamma^3}{2}, \quad V_p = (1 - \rho)V_\alpha + \rho V_\theta, \quad V_\theta = \frac{a_\theta b_\theta c_\theta}{12} \quad (3)$$

where, V_α , V_γ , V_p , and V_θ , are atomic volume of ferrite, austenite, pearlite and cementite. ρ is the phase fraction of cementite in pearlite. a , b and c are the lattice parameters of the respective phases. Many researchers have reported that the lattice parameter of each phase varies linearly with temperature and can be expressed with equations shown below:

$$a_\alpha = a_{\alpha,0} \{1 + e_\alpha (T - 298)\} \quad (4)$$

$$a_\gamma = a_{\gamma,0} \{1 + e_\gamma (T - 298)\} \quad (5)$$

$$a_\theta = a_{\theta,0} \{1 + e_\theta (T - 298)\} \quad (6)$$

$$b_\theta = b_{\theta,0} \{1 + e_\theta (T - 298)\} \quad (7)$$

$$c_\theta = c_{\theta,0} \{1 + e_\theta (T - 298)\} \quad (8)$$

where, a_i and a_{i0} are the lattice parameters of the each phase at a given

temperature and room temperature, and e_i is the linear thermal expansion coefficient of the each phase. T is the temperature in K. The dependence of the lattice parameter of ferrite and austenite on alloying elements was as reported by Bhadeshia et al [22]. and Dyson and Holmes [23], respectively.

$$a_{\alpha,0} = 2.8664 + \frac{(a_{Fe} - 0.279X_C)(a_{Fe} + 2.496X_C) - a_{Fe}^3}{3a_{Fe}^2} - 0.03X_{Si} \quad (9)$$

$$+ 0.06X_{Mn} + 0.07X_{Ni} + 0.31X_{Mo} + 0.05X_{Cr} + 0.096X_V$$

$$a_{\gamma,0} = 3.5780 + 0.033w_C + 0.00095w_{Mn} - 0.0002w_{Ni}$$

$$+ 0.0006w_{Cr} + 0.0056w_{Al} + 0.022w_N - 0.0004w_{Co} + 0.0015w_{Cu} \quad (10)$$

$$+ 0.0031w_{Mo} + 0.0051w_{Nb} + 0.0039w_{Ti} + 0.0018w_V + 0.0018w_W$$

where, X and w are the atomic and weight fraction of solute atoms denoted by the subscripts, respectively. Lattice parameters of cementite are constant values, and the value of $a_{\theta,0}$, $b_{\theta,0}$ and $c_{\theta,0}$ were 4.5246, 5.0885 and 6.7423Å, respectively [24]. e_{θ} was given as a polynomial function of temperature expressed by the equation that follow [24]:

$$e_{\theta} = 6.0 \times 10^{-6} + 3.0 \times 10^{-9}(T - 273) + 1.0 \times 10^{-11}(T - 273)^2 \quad (11)$$

The reported value of e_{α} and e_{γ} are $1.766 \times 10^{-5} \text{K}^{-1}$, $2.355 \times 10^{-5} \text{K}^{-1}$, respectively

[25]. However, there are some mismatches between measured data and reported coefficient of thermal expansion (CTE). Therefore, considering those mismatches, modified and recommended equations are as follow:

$$a_{\alpha} = a_{\alpha,0} \{1 + k_{\alpha} \cdot e_{\alpha} (T - 298)\} \quad (12)$$

$$a_{\gamma} = a_{\gamma,0} \{1 + k_{\gamma} \cdot e_{\gamma} (T - 298)\} \quad (13)$$

k_{α} and k_{γ} are CTE correction factor of ferrite and austenite, respectively. When there are no mismatches between measured data and reported value, those values are just 1.

2.3.2 Transformation plasticity model

Generally, it is known that nonisotropic volume changes in dilatometry were observed during the phase transformation, even in steel with an isotropic microstructure. The main reason of those phenomenon is non-isotropic volume change during phase transformation, and it makes additional permanent deformation during phase transformation. Therefore the contribution of non-isotropic volume change to the dilatation data is designated as a non-isotropic dilatation in the present study.

In this study, the transformation plasticity model proposed by Han *et al.*

[20] was adopted to explain the non-isotropic volume change during phase transformation. The mechanism of transformation plasticity is divided into diffusional and diffusionless phase transformation. First, the transformation plasticity during diffusional transformation is explained, when a stress is applied during the phase transformation, the migrating atoms move to release the applied stress field, inducing an atomic flux along the phase interface. Using this concept, a constitutive equation for the diffusional transformation plasticity was described as a function of the transformation rate (\dot{X}) and applied stress (σ_0):

$$\dot{\epsilon}^{TP} = \frac{1}{3} \frac{d_0}{\delta} \dot{X} \frac{(\sigma_0 + \sigma_x) \Omega}{k_B T} c_{v0} \exp\left(-\frac{Q_f}{k_B T}\right) \quad (14)$$

where σ_x is the constant of the transformation plasticity decided by dilatometric experiment, and d_0 is the initial grain size of the parent phase, δ is the effective thickness of the interface, Ω is the volume of the vacancy, c_{v0} is a dimensionless constant determined by the change in thermal entropy associated with the formation of vacancies, and Q_f is the formation enthalpy of the vacancy at the interface. The Boltzmann constant, k_B , has a value of 1.38×10^{-23} J/K. In this study, the initial grain size of the austenite phase was measured as 30 μm . Ω , δ , Q_f and c_{v0} were $1.21 \times 10^{-29} \text{ m}^3$ [26], 1 nm, 80

kJ/mol, and 1.2 [20], respectively.

In the diffusionless transformation, the anisotropic transformation strain is caused by the selectivity of some specific variants increased by the externally applied stress [21]. It was reported that the transformation strain increases almost linearly as the applied stress. Therefore, in order to explain the transformation plasticity during the martensite transformation, the linear model was adopted as follows:

$$\dot{\varepsilon}^{TP} = A\dot{X}(\sigma_0 + \sigma_x) \quad (15)$$

where the constant A was experimentally obtained as $2 \times 10^{-10} \text{ Pa}^{-1}$ [19].

2.3.3 Carbon enrich model

During the decomposition of austenite into ferrite in carbon steels, solute carbon is ejected from the ferrite, due to its solubility limit being exceeded, and is enriched into the untransformed austenite. This carbon enrichment increases the atomic volume of untransformed austenite, which makes the dilatation curve of austenite deviate from the linear line. Therefore, in this study, partitioning of C in $(\alpha+\gamma)$ region was considered, then carbon concentration in austenite phase, $X_{C\gamma}$, can be related by mass balance:

$$X_{C_\gamma} = \frac{X_{C_0} - (1 - f_\gamma)X_{C_\alpha}}{f_\gamma} = \frac{X_{C_0} - f_\alpha X_{C_0}}{1 - f_\alpha} \quad (17)$$

where f_α , f_γ , X_{C_0} , and X_{C_α} are fraction of the ferrite and austenite phase, the carbon concentrations of the entire specimen and ferrite, respectively. The maximum value of carbon concentration in the ferrite was concerned with the carbon solubility of ferrite which is obtained by thermodynamic calculation [27]. The thermodynamic equilibrium value when $(\alpha+p)$ transforms to $(\alpha+\gamma)$ was used then X_{C_γ} can be obtained as a function f_γ . Consequently, V_γ becomes a function of f_γ as the lattice parameters have a term including carbon concentration. Therefore, the equation (10) becomes a non-linear equation of f_γ and this should be solved numerically.

As shown at Fig. 5, the 3 models, lattice parameter based strain calculation, transformation plasticity model, carbon enrich model, are non-linearly coupled to analysis the transformation behaviors of the steel. The error value is the difference between the measured and calculated strain, and the model automatically modified the phase fraction and TP constant, $\sigma\alpha_0$, to minimize the error value.

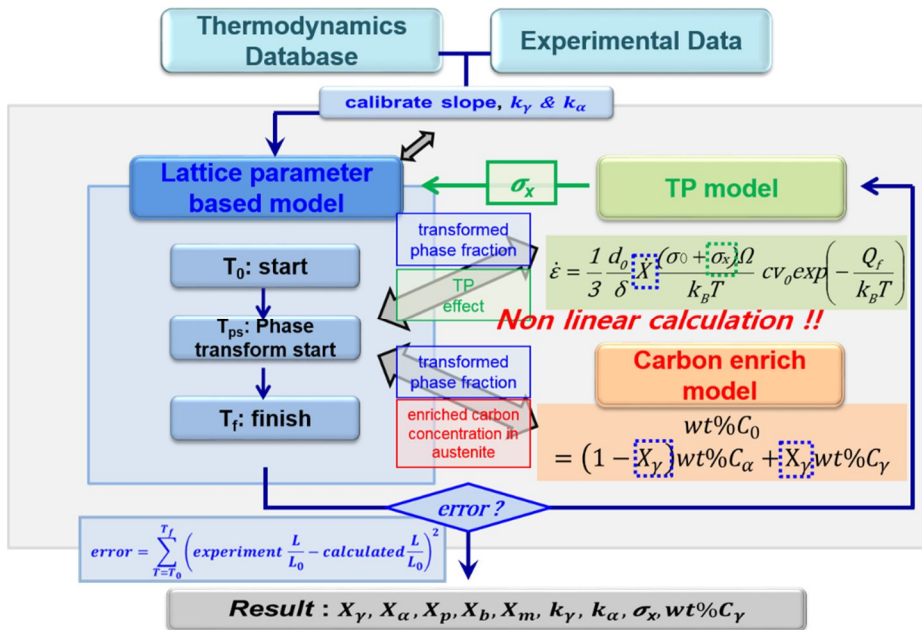


Figure 5

2.4 Results and discussion

Fig. 6a shows the compares the measured and analyzed dilatometric curves of the LMn steel during heating to 950 °C and cooling to room temperature. The heating and cooling rates were 10 °C/sec and 0.5 °C/sec as in the case of Fig. 4a. To minimized the error developed analyze method was used so temperature-strain graph has been reconstructed. As shown in this figure, developed analyze method has a good agreement with measured dilatation graph, and it proves the accuracy of this method. This method is also verified by comparing the results with that of classical Lever rule method at Fig. 6b. Fig. 6b shows change of austenite phase fraction due to temperature decline. As shown at this figure, fraction of austenite start to decrease at near 700 °C during cooling stage due to formation of ferrite structure. This result is observed in both classical Lever rule method (black line) and developed method (red line). Developed method includes thermodynamic data which contains solubility of carbon and formation start temperature of each phases, and we can distinguish the type of BCC structure using this data. As shown at Fig. 6c, transformed BCC phase fraction is divided into ferrite and pearlite structure using the ae_3 and ae_1 temperature based on para equilibrium phase diagram. In this method, the transformed phase fraction existing above ae_1 temperature is assumed to be ferrite

structure, and the fraction existing under the ael temperature is assumed as pearlite structure. The final fraction of each structure, error correction factor, k_γ , k_α , and transformation plasticity constant, σ_x , are listed at Table 2. Using the microstructural observation shown at Fig. 6d, we can define the real final structure of this condition, and verify the phase distinguish assumption in Fig 6c. Fig. 7a shows the comparisons between the measured and analyzed dilatometric curves of the LMn steel with relatively fast cooling rates - 20 °C/sec. Measured (black line) and analyzed (red line) results also show good agreement, and this graph shows phase transformation near 400 °C, which is relatively low temperature compared as Fig. 6a. The type of transformed BCC structure also distinguished using the analyzing method and empirical equations concerning thermodynamic transformation start temperature. As shown at Fig 7b, the transformed phase which exists under bainite start temperature and above martensite start temperature is assumed as bainite structure and the transformed phase below the as martensite start temperature is assumed martensite structure. The final fraction of each structure, error correction factor, k_γ , k_α , and transformation plasticity constant, σ_x , are also listed at Table 2, and final fraction of microstructure is confirmed using optical micro structure at Fig 7c.

Fig. 8a shows the comparisons between the measured and analyzed dilatometric curves of the HMn steel during heating to 950 °C and cooling to room temperature. The heating and cooling rates were 10 °C/sec and 20 °C/sec

as in the case of Fig. 1a. Phase transformation from FCC to BCC occurs at relatively very low temperature of near 200 °C due to the addition of Mn which is the strong austenite stabilizer. Analyze of transformed BCC type shown at Fig 8b and micro structural observation at Fig 8c also show this martensite formation at low temperature. The final fraction of each structure, error correction factor, k_γ , k_α , and transformation plasticity constant, σ_x , are also listed at Table 2.

Fig. 9 shows the comparisons between the measured and analyzed dilatometric curves of the HMn steel with various holding temperature between a_{e3} and a_{e1} temperature. The heating and cooling rates were 1 °C/sec and 20 °C/sec and holding temperature 650, 670, 690 °C as in the case of Fig. 2b. The relationships between temperature and strain show drastic changes due to small difference of holding temperature, therefore, analysis of dilatation data considering retained austenite had to be performed in order to obtain reasons of those phenomenon. Fig. 10 shows change of phase fraction during heating process using the developed method. The transformation plasticity parameter, σ_x , is the the same as the result of Fig 8a which is held 950 °C and transformed full martensite structure during cooling. As shown at Fig. 8, when holding temperature is 650 °C, there is very small fraction of austenite after holding stage. However, when the holding temperature is increased up to 670 °C and 690 °C, the fraction of austenite is also increased up to 64.2% and 81.8%. After the holding stage, austenite phase is transformed to martensite

following cooling stage as shown at Fig 11. When the holding temperature is 650 °C, there is very small phase transformation of austenite to martensite due to the very small amount of pre-existing austenite during holding stage. When the holding temperature is 670 °C, although there is enough to transform pre-existing austenite during holding stage, there is only 3.2% of phase transformation of austenite to martensite. The main reason for this result is the decrease of the martensite start temperature due to enrichment of strong austenite stabilizer such as C and Mn. However, when the holding temperature is 690 °C, there is considerable phase transformation of austenite to martensite during cooling stage. The main reason for this phenomenon is the difference of pre-existing austenite fraction during holding stage. The fraction of pre-existing austenite is the highest when the holding temperature is 690 °C, therefore the degree of enrichment is the lowest. Consequently, the decrease in martensite start temperature is not big enough to drop under the room temperature. Fig. 12 shows the phase map of those 3 conditions using EBSD measurement. Measured and analyzed fraction have a good agreements and the detailed results is arranged at Table 3.

Table 2.

steel	Cooling rate (°C/sec)	k_γ	k_α	austenite	ferrite	pearlite	bainite	martensite	TP constant
LMn_steel	0.5	1.11	0.97	0	0.85	0.15	0	0	0.62
LMn_steel	20	1.22	0.99	0	0	0	0.55	0.45	0.62
HMn_steel	20	1	1.05	0.03	0	0	0	0.97	0.87

Table 3.

Holding temp (°C)	Fraction of FCC			Fraction of BCC		
	Dilatometric analysis	XRD	EBSD	Dilatometric analysis	XRD	EBSD
650	1.1	0.1	0.6	98.9	99.9	99.4
670	64.2	54.7	65.5	35.8	45.3	34.5
690	18.2	11.1	15.8	81.8	88.9	84.2

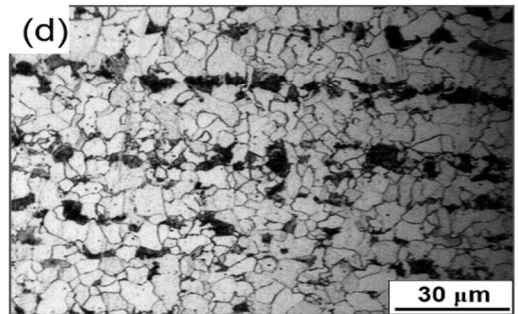
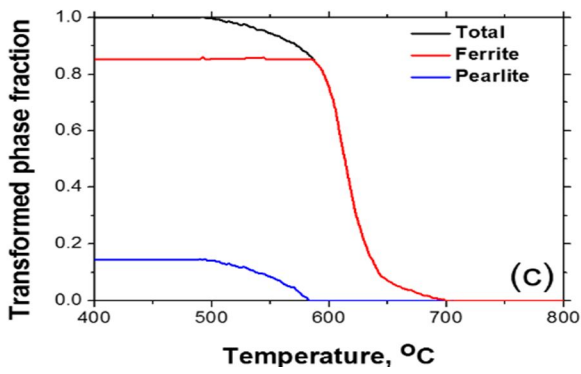
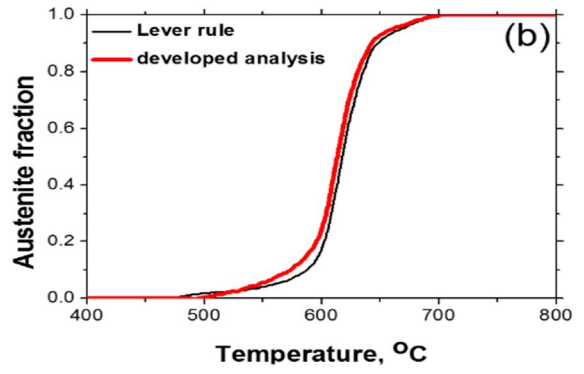
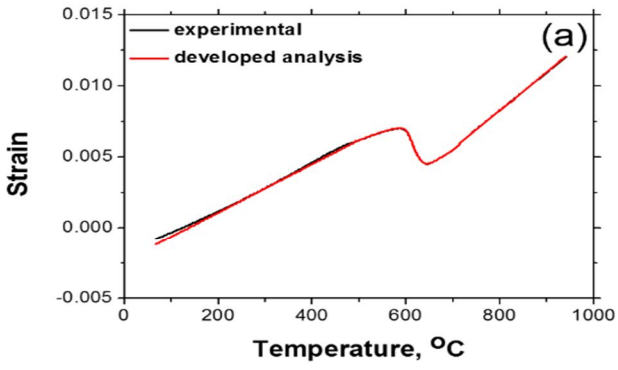


Figure 6

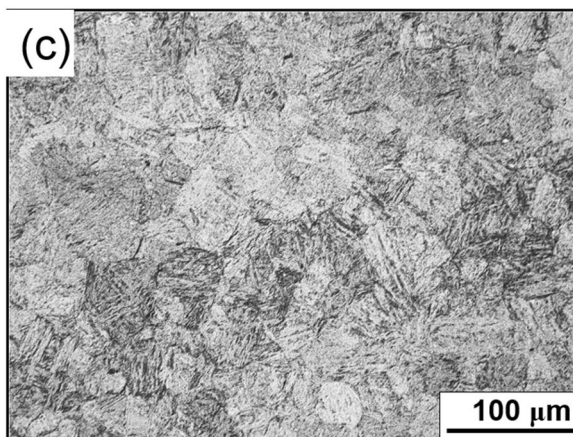
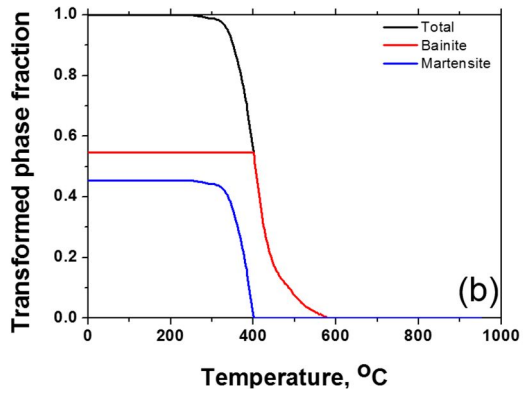
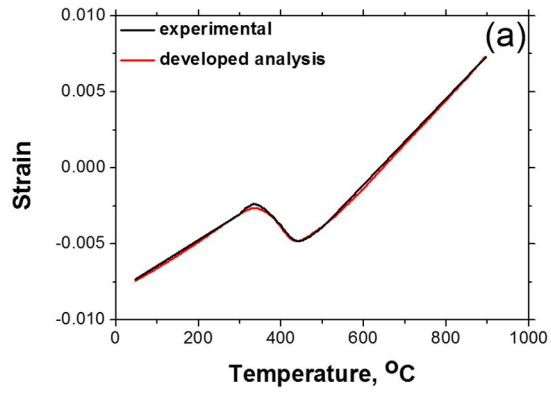


Figure 7

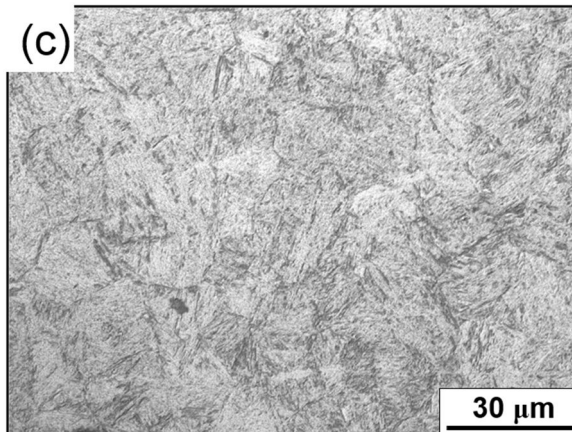
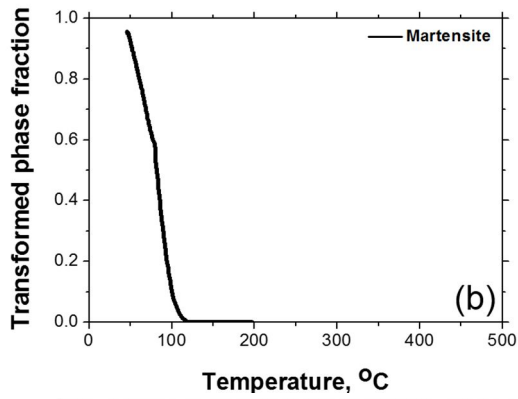
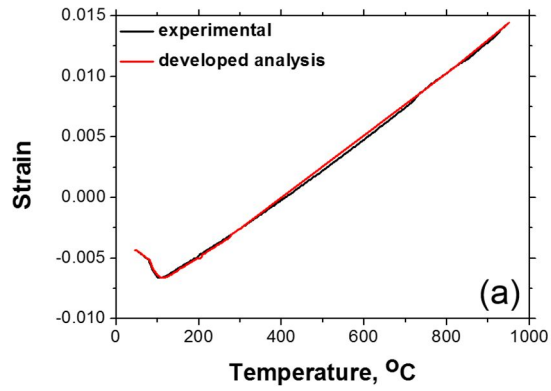


Figure 8

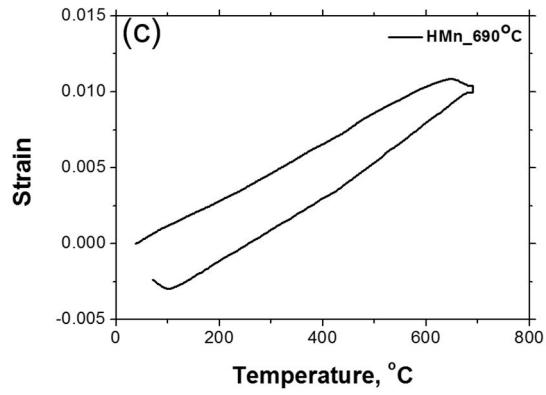
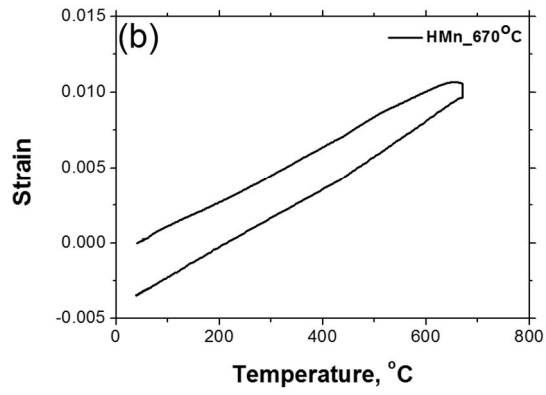
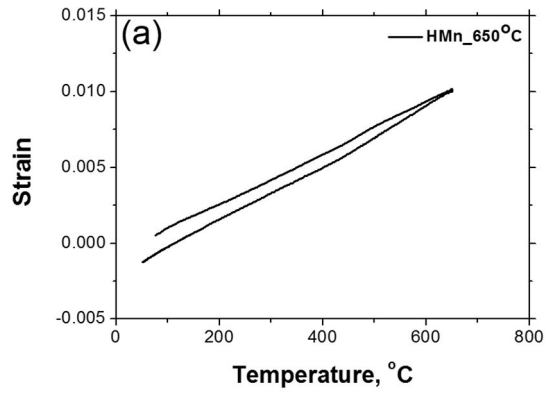


Figure 9

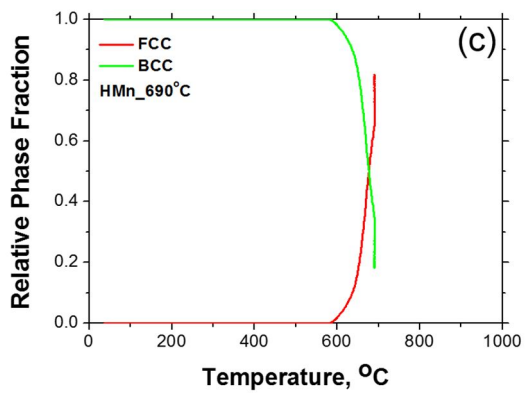
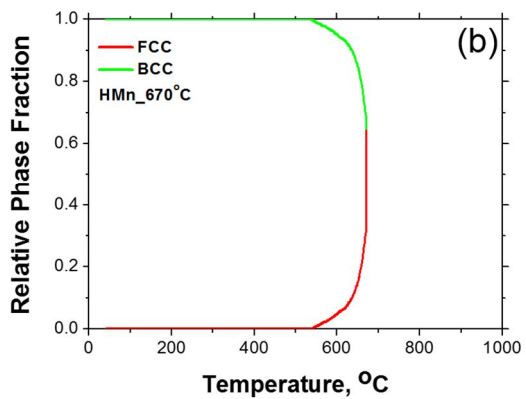
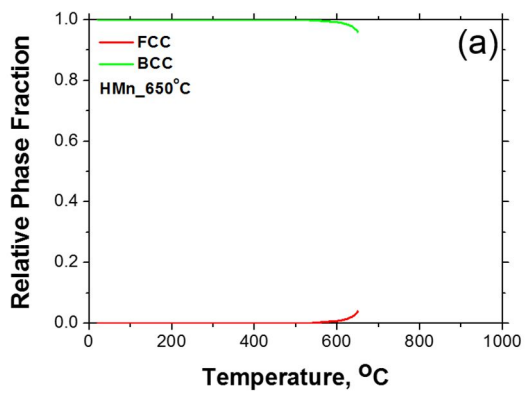


Figure 10

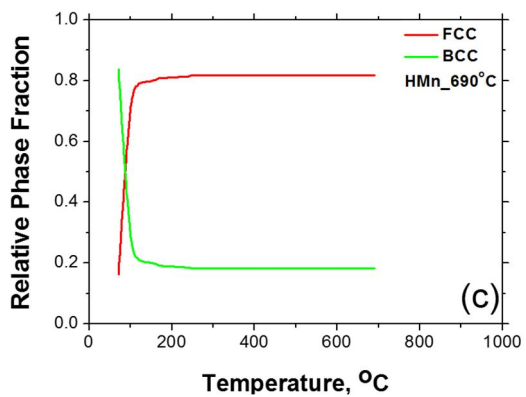
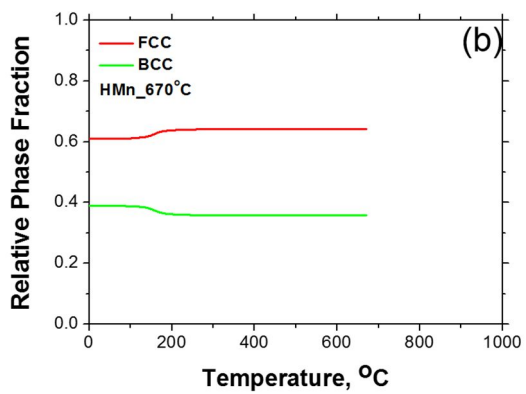
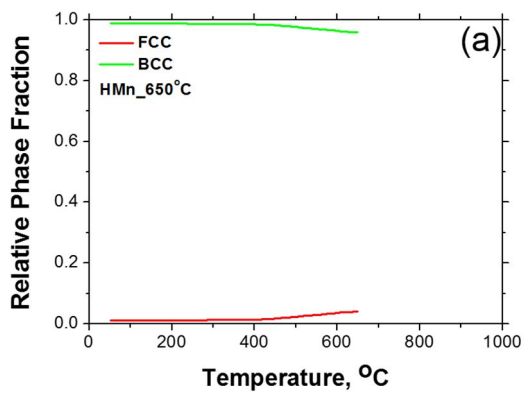


Figure 11

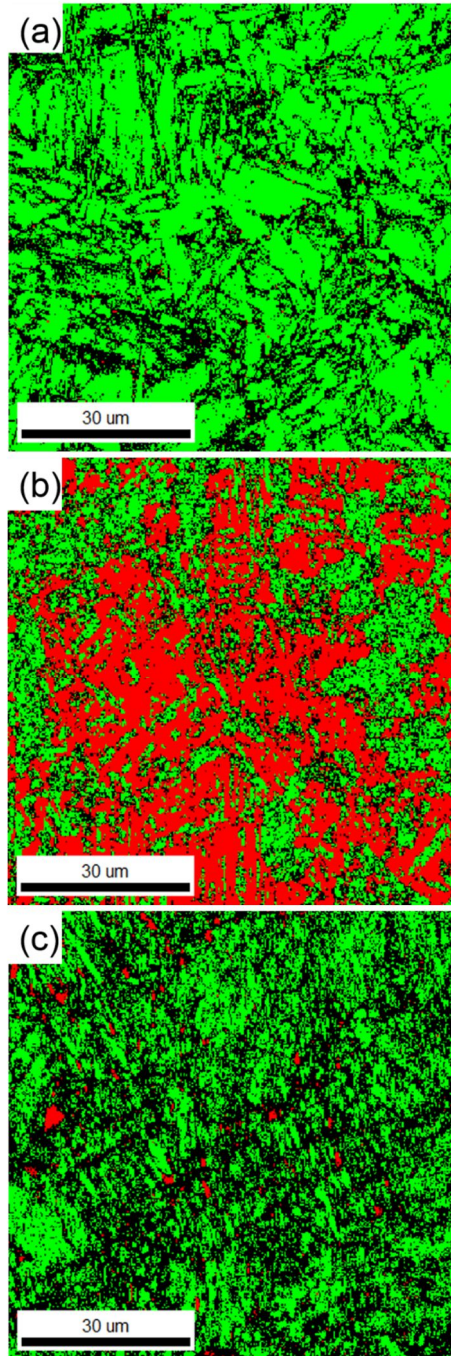


Figure 12

2.5 Conclusion

This paper studied the method of dilatometric analysis to analyze the phase transformation behaviors of AHHS with retained austenite. Developed dilatometric analysis method is based on lattice parameter and atomic volume of each phase and additionally considers transformation plasticity and enrich of alloying element. Using the thermodynamic data and equations embedded in the method, it can distinguish the type of BCC structure. Analysis of two specimens which has different Mn, the strong austenite stabilizer, we can verify the accuracy of developed method and find various parameters concerning transformation plasticity and fraction of retained austenite. This method is preferred to obtain the fraction of final fraction of retained austenite very simply and phase transformation kinetics of retained austenite steel.

2.5 References

- [1] H. Aydin, E. Essadiqi, I.-H. Jung, S. Yue. *Mater. Sci. Eng. A* 564 501-508 (2013)
- [2] H.N. Han, C.-S. Oh, G. Kim, O. Kwon, *Mater. Sci. Eng. A* 499 462-468 (2009)
- [3] R.H.Wagoner, Report: Advanced High-Strength Steel Workshop, Arlington, Virginia, USA, October 22–23, 2006.
- [4] D.K. Matlock, J.G. Speer, Proceedings of the Third International Conference on advanced Structural Steels, 2006, pp. 774–781.
- [5] O. Kwon, S.-K. Kim, G. Kim, Proceedings of the 21st Conference on Mechanical Behaviors of Materials, Changwon, Korea, October 18–19, 2007.
- [6] H.K.D.H. Bhadeshia, R.W.K. Honeycombe, *Steels: Microstructure and Properties*, Elsevier, Butter worth–Heinemann, Amsterdam, Boston, 2006
- [7] S.Keeler (Ed.), in: Proceedings of the Advanced High Strength Steel (AHSS) Application Guidelines, 2009.
- [8] Y. Weng, H. Dong, Y.X. Gan, Springer, Metallurgical Industry Press, Berlin, Heidelberg, New York, 2011S. 1.

- [9] D.K. Matlock, J.G. Speer, Third generation of AHSS: microstructure design concepts, in: A. Haldar, S. Suwas, D. Bhattacharjee(Eds.), Proceedings of the International Conference on Microstructure and Texture in Steels, Springer, London, 2009, pp.185–205.
- [10] H. Aydin, H.K. Zeytin, H. Cimenoglu, Effect of micro alloying elements and deformation mechanisms on the twip steels, in :S.M. Howard(Ed.), Epd Congress 2009, Proceedings, 2009, pp.191–197.
- [11] E. De Moor, J.G. Speer, D.K. Matlock, J.-H. Kwak, S.-B. Lee, Steel Res. Int. 83 322–327 (2012)
- [12] J.-Y. Kang, D.H. Kim, S.-I. Baik, T.-H. Ahn, Y.-W. Kim, H.N. Han, ISIJ Int. 51 130–136 (2011)
- [13] J.-Y. Kang, S.J. Park, D.-W. Suh, H.N. Han, Mater. Charact. 84 205-215 (2013)
- [14] M. Apel, S. Benke, I. Steinbach, Comput. Mater. Sci. 45 589-592 (2009)
- [15] M. Jung, M. Kang, Y.-K. Lee, Acta Mater. 60 525-536 (2012)
- [16] Y.-G. Cho, Y.-R. Im, J.K. Lee, D.-W. Suh, S.-J. Kim, H.N. Han, Metall. Mater. Trans. A. 42A 2094-2106 (2011)
- [17] D.-W. Suh, C.-S. Oh, H.N. Han, S.-J. Kim, Acta Mater. 55 2659-2669 (2007)
- [18] H.N. Han, J.K. Lee, ISIJ Int. 42 200-205 (2002)

- [19] H.N. Han, C.G. Lee, C.-S. Oh, T.-H. Lee, S.-J. Kim, *Acta Mater.* 52 5203-5214 (2004)
- [20] H.N. Han, J.K. Lee, D.-W. Suh, S.-J. Kim, *Philos. Mag.* 87 159-176 (2007)
- [21] H.N. Han, D.-W. Suh, *Acta Mater.* 51 4907-4917 (2003)
- [22] H.K.D.H. Bhadeshia, S.A. David, J.M. Vitek, R.W. Reed, *Mater. Sci. Technol.* 7 686–98 (1991)
- [23] D.J. Dyson, B. Holmes, *J. Iron Steel. Inst.* 208 469–474 (1970)
- [24] H. Stuart, N. Ridley, *J. Iron Steel. Inst.* 204 711–717 (1966)
- [25] M. Onink, F.D. Tichelaar, C.M. Brakman, E.J. Tittemeijer, *Z Metallkd* 87 24–32 (1996)
- [26] H.J. Frost, M.F. Ashby, *Deformation Mechanism Maps, The Plasticity and Creep of Metals and Ceramics.* Pergamon Press, 1982, pp. 21.
- [27] B. Sundman, B. Jansson, J.O. Andersson, *CALPHAD.* 9 153–190 (1985)

Chapter 3

A model for phase transformation of microalloyed low carbon steel combined with Nb precipitation kinetics

3.1 Introduction

In recent years, for automotive applications, the need for new advanced high strength sheet steels (AHSSs) with high ductility has rapidly increased. This is related to the need for more fuel-efficient cars, reduction of CO₂, and increasing consumer demand for safer vehicles. The microalloyed AHSSs has lately attracted considerable attention for this automotive application.

The microstructural evolution during manufacturing process affects the material properties of the steel products. In the Nb-added microalloyed AHSSs, especially, it is known that controlling precipitation kinetics of Nb play a critical role in phase transformation behavior of the steel [1-3]. Therefore, in order to develop a microalloyed AHSS with the appropriate strength-ductility balance, both precipitation and phase transformation kinetics should be considered simultaneously.

As for the measurement of precipitation, there were many attempts

using various experimental methods such as transmission electron microscopy (TEM) [4], electrolytic dissolution [5], hot compression [6,7], hot torsion [8] and electrical resistivity method [9]. However, determining precipitation behavior using experimental method has a limitation with respect to need too many experimental procedures.

In order to overcome the limitation, there were many approaches to model precipitation behavior. Fratzl *et al* [10]. modeled this behavior using Monte Carlo simulations of Ising model. While this approach gives important details of the diffusion and precipitation processes, this approach detailed extremely for a description of multi-component, multi-particle, multi-phase processes, thus their model was far to be applied to many particles system in the point of time-consuming.

Therefore a new model was developed, based on application of the Onsager extremum principle within a mean field approach, which simultaneously keeps the complexity and the promptitude [11]. Using those developed models, Kozeschnik *et al.* developed the thermo-kinetics software package Matcalc, which can calculate simulation of the precipitate evolution [12,13].

The phase transformation behaviors of the steels were characterized by Johnson-Mehl-Avrami-Kolmogorov (JMAK) type equations and measured by dilatometric analysis [14-16]. When a phase transformation occurs during solid state, the dilatation curve provides information on the resulting atomic

volume change, as well as the thermal expansion of the steels. The volume fraction of the individual phase is determined by the application of a lever rule to the dilatation curve [17]. Many researchers have provided modified analysis methods considering carbon enrichment in austenite [18] and nonisotropic volume change of the steels [19-21]. However, in previous models, they had no regard for precipitation effect of alloying element and assumed entire Nb in steels are solid solution state.

In this study, numerical simulation of precipitate evolution in austenite range of low carbon Nb microalloyed steels during various heat treatments is carried out by the commercial thermo-kinetic software package MatCalc (ver.5.44). Comparing between calculated precipitation behaviors and measured data using TEM observation, we verifies the accuracy of this model. In order to determine the effect of precipitation concerning phase transformation behavior, Nb is divided into two groups, solid soluted Nb and precipitated Nb, based on Matcalc calculations. After that, phase transformation behaviors are measured by dilatometric analysis and those behaviorss are modelled on the basis of a Johnson–Mehl–Avrami–Kolmogorov (JMAK) equation modified to consider precipitation effect.

3.2 Experimental procedure

The Nb-microalloyed steels, which is the chemical composition of the steel is listed in Table 1, were melted by a high-frequency vacuum induction furnace and were cast into a metallic mold. The 100 mm ingot was homogenized in a protective atmosphere at 1200 °C for 1 hour and hot rolled into a plate of about 6 mm thick. As shown at Fig. 1, the specimens were austenitized 1250 °C for 900 seconds to dissolve the pre-existing Nb precipitate, secondly the specimens were soaked at 865, 915, 965 °C for 10 to 300 min and quenched in order to investigate precipitation behaviors using TEM (JEOL, JEM-3000F) observation. The specimens for TEM observation were prepared by carbon extraction replica. Nanometer-sized Nb precipitates extracted onto copper mesh grids were measured using a high-resolution TEM equipped with an EDS with a spot size as small as 3 nm.

Fig. 2 shows heat treatment condition to analyze phase transformation behaviors by dilatometric method. The dilatometric measurement was performed using a quench dilatometer (R&B, TM-111129-001), which heats the specimen with an induction coil and detects the length change along L direction with a linear variable displacement transducer. The temperature of the specimen was monitored with a K-type thermocouple attached to the specimen surface and dilatometric specimens of the cylindrical type, 3 mm in

diameter and 10 mm in length, were prepared. We conducted two types of different heat treatment conditions controlling pre-cipitation behaviors and fixing other experimental variables. Dilatometric analysis listed in Fig. 2a were conducted, the dilatometric specimens were heated to 1000 °C at the heating rate of 10 °C /s then austenitized for 5 minute followed by cooling to room temperature at the cooling rates of 1 °C /s. This condition had not a sufficient reaction time to form precipitates, therefore the great part of Nb is still remains in solid solute state. Another dilatometric experiment which has additional soaking time at 850 °C for 3 hours is shown at Fig. 2b. In this condition, most of solid soluted Nb were changed into precipitates during enough soaking treatment.

Table 1.

	C	Si	Mn	S	Cr	Nb	N	Al
Steel_#1	0.1	0.1	1.7	0.003	0.1	0.04	0.003	0.05
Steel_#2	0.1	1.5	1.7	0.003	0.1	0.04	0.003	0.05

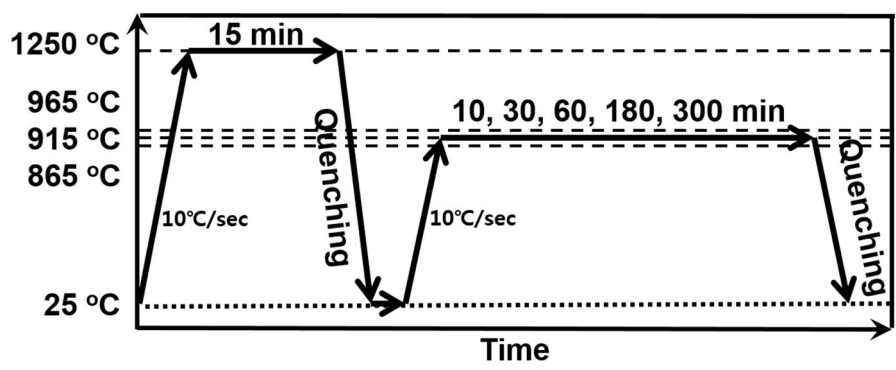


Figure 1.

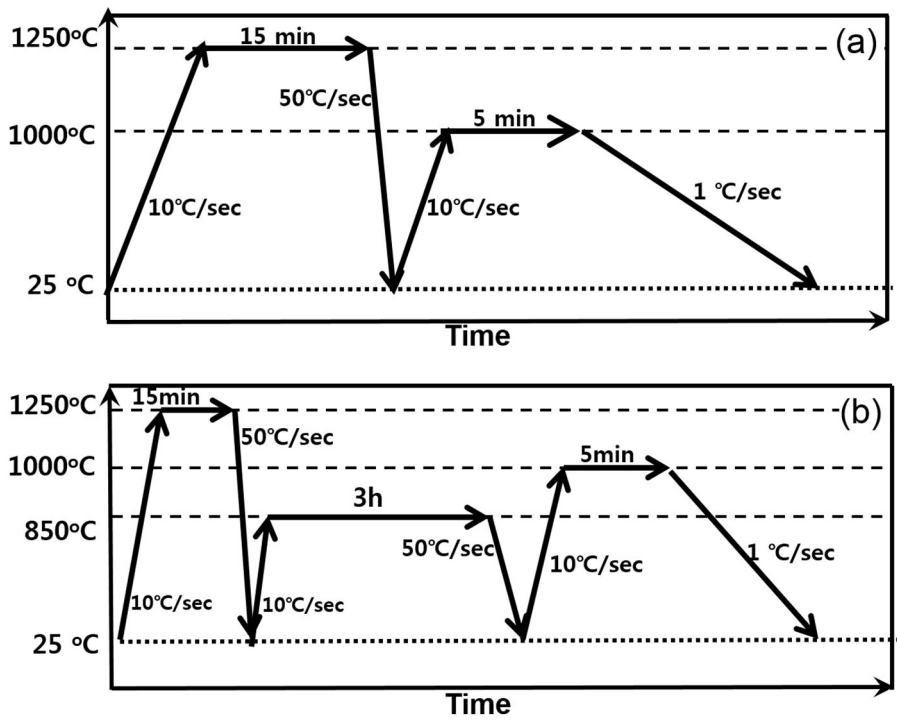


Figure 2.

3.3 Model development

3.3.1 Precipitation Model

For the precipitation simulations, the thermo-kinetics software MatCalc [12,13] and the corresponding databases 'mc_steel' is used. In this model, the evolution of the thermodynamic system is simulated based on the Kampmann-Wagner (KWN) model [22] which assumes the total time history is broken into adequately small, isothermal segments. Precipitates are grouped in classes and the evolution of radius and chemical composition is calculated according to the rate equations derived from the thermodynamic extremum principle [11].

In this approach, the nucleation kinetics of precipitates are calculated from the classical nucleation theory (CNT) [23] extended for multi-component systems [12,13]. The nucleation rate, J , is given by this theory as follow:

$$J = N_0 Z \beta^* \cdot \exp\left(\frac{-G^*}{k \cdot T}\right) \cdot \exp\left(\frac{-\tau}{t}\right) \quad (1)$$

where, N_0 is the number of potential nucleation site which is affected by

dislocation density and grain size, T is the temperature, k is the Boltzmann constant and t is the time. Z is the Zeldovich factor which accounts for the decay of some of the supercritical clusters. The atomic attachment rate β^* takes into account the long-range diffusive transport of atoms, which is needed for nucleus formation if the chemical composition of the matrix is different from the chemical composition of the precipitate. The incubation time, τ , represents the time taken to establish the initial cluster distribution and G^* is the critical energy for nucleus formation [23,24].

Using the assumption of a spherical nucleus, the Z , β^* and τ values may be

$$Z = \frac{V_\alpha (\Delta G_{vol} - \Delta G_s)^2}{8\pi \sqrt{\gamma^3 kT}} \quad (2)$$

$$\beta^* = \frac{16\pi\gamma^2 cD}{(\Delta G_{vol} - \Delta G_s)^2 a^4} \quad (3)$$

$$\tau = \frac{1}{2\beta^* Z^2} \quad (4)$$

Where, V_α is the volume per atom in the matrix, c is the concentration atomic fraction of solute in the matrix, a is the lattice constant of the product phase and D is the diffusivity of the solute in the matrix. γ is the effective interfacial

energy, ΔG_{vol} represents the volume free energy change and ΔG_s represents the misfit strain energy, respectively.

The critical energy for nucleus formation G^* is also as follow [23]:

$$G^* = \frac{16\pi}{3} \frac{\gamma^3}{(\Delta G_{vol} - \Delta G_s)^2} \quad (5)$$

It is important that G^* is the most essential quantity in nucleation theory, when compared with the other quantities occurring in equation (1). G^* contains the cube of the interfacial energy over the square of the effective driving force $\Delta G_{vol} - \Delta G_s$. Since G^* appears in the exponent of the nucleation rate equation (1). Therefore, small differences in the interfacial energy can therefore lead to large variations in the predicted nucleation rate, and this constitutes one of the main sources of error in the KWN model.

In order to determine exact interfacial energy, the concept of generalized nearest-neighbor broken-bond (GGB) model [25] was used extended concept of classical nearest-neighbor broken-bond approach [26]. In this approach, the interfacial energy γ_0 of a planar, sharp phase boundary has been expressed as follows:

$$\gamma_0 = \frac{n_s \cdot z_{s,eff}}{N \cdot z_{L,eff}} \Delta E_{sol} \quad (6)$$

where $z_{L,eff}$ is effective number of broken atomic bond across the interface, $z_{S,eff}$ is the effective coordination number. N is the Avogadro constant, n_S represents the number of atoms per unit interface area. The solution enthalpy is represented by ΔE_{sol} . Energy contributions from misfit strains in the interface are neglected in this approach. However this model is inappropriate for small having high interface curvature, therefore we use size-correction expression to take this effect into account [27].

The details of the calculation condition are as below. The matrix phase defined in the simulation is austenite. The grain size of austenite was measured 30 μm and the dislocation density of the austenite matrix was assumed to be 10^{-10} m^{-2} . The interfacial energy between the precipitate and the matrix was calculated based on nearest-neighbor broken-bond model and it was reduced by 2.5 % to predict appropriate interfacial energy considering coherency effect [27].

3.3.2 Phase Transformation Model

The transformed phase fraction, X , during isothermal austenite decomposition has been characterized using the JMAK type equation [28] as follows:

$$X = X^e \left[1 - \exp(-kt^n) \right] \quad (7)$$

where X^e is the thermodynamic equilibrium fraction, which can be determined from the equilibrium phase diagram at a given chemical composition and temperature, t is the total time for transformation. The rate constant k depends on the temperature, chemical composition, austenite grain size and precipitation behaviors. The time exponent n is a constant over the temperature range when a chemical composition of steel is determined.

In order to extend the JMAK equation for phase transformation to the nonisothermal condition, the concept of additivity rule [29], which is based on the theory of Scheil [30], was introduced under the assumption that the cooling curve can be divided into small time intervals within which the kinetics values remain constant. The transformed phase fraction until the i th step, X_i , is expressed as follows:

$$X_i = X_i^e \left\{ 1 - \exp \left[-k_i (t' + \Delta t)^n \right] \right\} \quad (8-1)$$

$$t' = \left[-\frac{1}{k_i} \ln \left(\frac{1 - X_{i-1}}{X_i^e} \right) \right]^{1/n} \quad (8-2)$$

where t' is equivalent transformation time needed to transform into the fraction of X_{i-1} at the temperature of the i th step, and Δt is the time step corresponding to the i th step. The values, k and n were determined from the dilatation data obtained by the continuous cooling tests using an inverse additivity technique. The k and n values of the austenite to ferrite, widmanstatten ferrite, pearlite and bainite transformations are listed on Table 2, respectively. In this table, k and n values are made of function of chemical composition, austenite grain size and temperature. C is the carbon content in untransformed austenite, Si represents the silicon content, respectively. Nb is divided into two parts, soluted Nb and precipitated Nb, AGS (μm) means the prior austenite grain size.

Table 2.

	k	n
	$[38.59 - 18.98[\%C]^{0.5} + 11.13[\%C] + 2.83[\%Si]^{0.99}$	
Austenite to Ferrite	$-18.21[\%solved Nb]^{0.81} + 2.94\log((ae3 - t)/ae3) + (- 27.85) * 1000.0 / t] * (2.521/[AGS] + 0.603[\%precipitated Nb])^{0.65}$	
Austenite to W. Ferrite	$[36.24 - 1.28[\%C]^{0.5} - 36.71[\%C] + 7.75[\%Si]^{0.97} - 23.93[\%solved Nb]^{0.9} + 5.24\log((ae3 - 50-t)/ae3) + (- 21.69) * 1000.0 / t] * (2.521/[AGS] + 0.603[\%precipitated Nb])^{0.28}$	0.9665 +
Austenite to Pearlite	$[29.02 - 5.03[\%C]^{0.5} + 62.34[\%C] + 1.95[\%Si]^{1.21} - 6.84[\%solved Nb]^{0.59} + 3.04\log((ae1 - t)/ae1) + (- 18.19) * 1000.0 / t] * (2.521/[AGS] + 0.603[\%precipitated Nb])^{0.45}$	1.7506[\%C]
Austenite to Bainite	$52.26 - 23.81[\%C]^{0.5} + 52.31[\%C] + 5.49[\%Si]^{1.09} + 0.121[\%solved Nb]^{0.79} + 5.69\log((ae3 - t)/ae3) + (- 11.84) * 1000.0 / t$	

3.4. Results and discussion

In order to observe relative fraction of precipitates size and composition measurement of precipitates, TEM observation and EDS analysis are conducted. Fig. 3 represents the precipitates of the steel_1 soaked at 865 °C during 10 to 300 min. The precipitates soaked during 10 min, represented in Fig. 3a, are in nucleation stage. The most of precipitates are ultrafine precipitates whose radius is under 2 nm, and few precipitates reached growth stages and their radius are larger than 2 nm. The mean radius of precipitates is 3.4 nm at this soaking time, and relative fraction of precipitates was 15% as compared with equilibrium precipitation fraction at 865 °C. Over the time, the precipitates reached growth stage and coarsening stage. In the growth stage, the phase fraction increases until the equilibrium phase fraction when respective temperature is reached. When the equilibrium phase fraction is reached, precipitation coarsening follows. This stage is characterized by a further growth of large precipitates at the expense of smaller ones by nearly constant phase fraction. Therefore, as listed at Table 3, radius and relative phase fraction of precipitates are increased simultaneously with the course of time. However if they reached the coarsening stage, the radius of precipitates remains to increases while the increase of relative phase fraction remains constant. Fig. 4 shows the effect of soaking temperature and Si on precipitation. Figs. 4a and b represent the precipitates of steel_2 having 0.1%

Si and steel_1 having 1.5 wt% Si, respectively. They were soaked at 865 °C for 10 min. As shown at Fig. 4a, precipitates with low Si concentration consists very small nanosized precipitates at the same temperature. Figs. 4c and d show the temperature effect on Nb precipitation. Nb precipitation is activated at the most 865 °C. The high resolution TEM image, diffraction pattern, EDS data of Nb precipitates are also confirmed at Fig. 5.

Fig. 6 shows the calculated precipitation behavior of Nb using MatCalc. The changes in relative phase fraction of precipitates are represented with a function of chemical composition of steels, soaking temperature, and soaking time, and they show a good agreement with the measured values, which is obtained by a TEM observation. According to the calculation result with the equation (1), addition of Si decreases energy barrier of nucleation, thus the reaction of steel_1 happened more rapidly since it contains more Si which leads to the increase of the nucleation rate. As shown at Fig. 5, the precipitation kinetics are the fastest at 865 °C and the slowest at 965 °C. Therefore, steel_1 soaked at 865 °C for 300 min has already reached the coarsening stage, while, steel_1 soaked at 965 °C during 300 min was still growth stage.

Fig. 7 shows the effect of dislocation density, grain size, and interfacial energy during Nb precipitation. Changes of grain size and dislocation density inflict very small changes in precipitation behaviors, but changes in interfacial energy cause significant changes on precipitation behaviors. This

phenomenon is caused by the cubic relationship between interfacial energy and critical energy for nucleus formation (G^*), therefore we can find the relationship between Si composition and precipitation behaviors using interfacial energy and G^* .

As shown at Fig. 8, Steel_1 with higher Si concentration has larger interfacial energy than steel_2, but, as shown at Fig. 9a, volume free energy change on nucleation formation is also large in Steel_1; these two parameters compete for the G^* . Considering these two parameters, G^* is smaller for steel_2 with low Si concentration, which becomes the main reason for hindrance in precipitation at low Si concentration. Considering those effect, we can predict relative precipitation behaviors and precipitation-time-temperature graph, and those results are listed in Fig. 10.

Figs. 11 shows the comparisons between the measure and calculated phase transformation behaviors considering Nb precipitation effect. There are two different results concerning Nb precipitation: solid solution effect (represented in line and square at Fig. 11) and precipitation effect (represented dash and triangle at Fig. 11). Nb in solid solution increases hardenability of steels and impedes austenite decomposition. In contrast, precipitated Nb functions as nucleation site for precipitation and accelerates austenite decomposition. Therefore the specimen with precipitated Nb has lower Ae3 temp and faster transformation behaviors than that with solid soluted Nb. Calculated phase transformation results are predicted based on JMAK equation and the values

are listed at Table 2. They have a good agreement with dilatometric analysis. Fig. 12 shows the effect of Si on phase transformation without Nb precipitation; addition of Si raises A_{e3} temperature and suppress bainite transformation. Thus steel_1 transforms into ferrite phase in early stage during slow cooling rate, and transform into bainite phase at lower temperature during fast cooling rate.

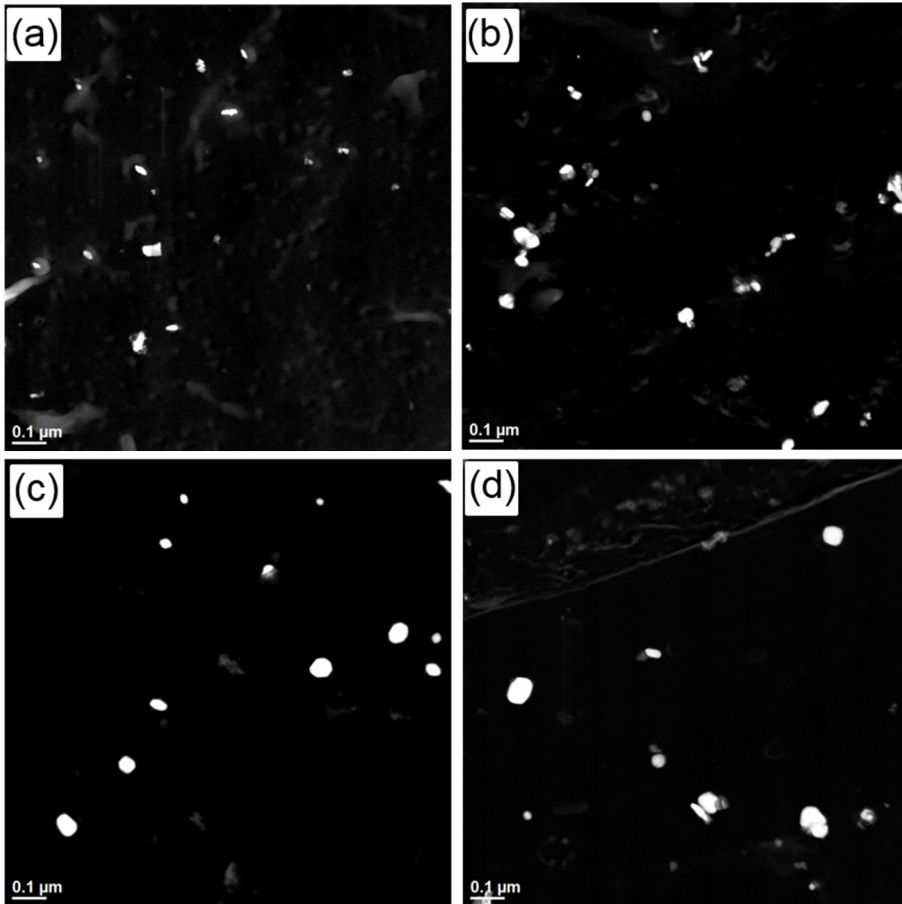


Figure 3.

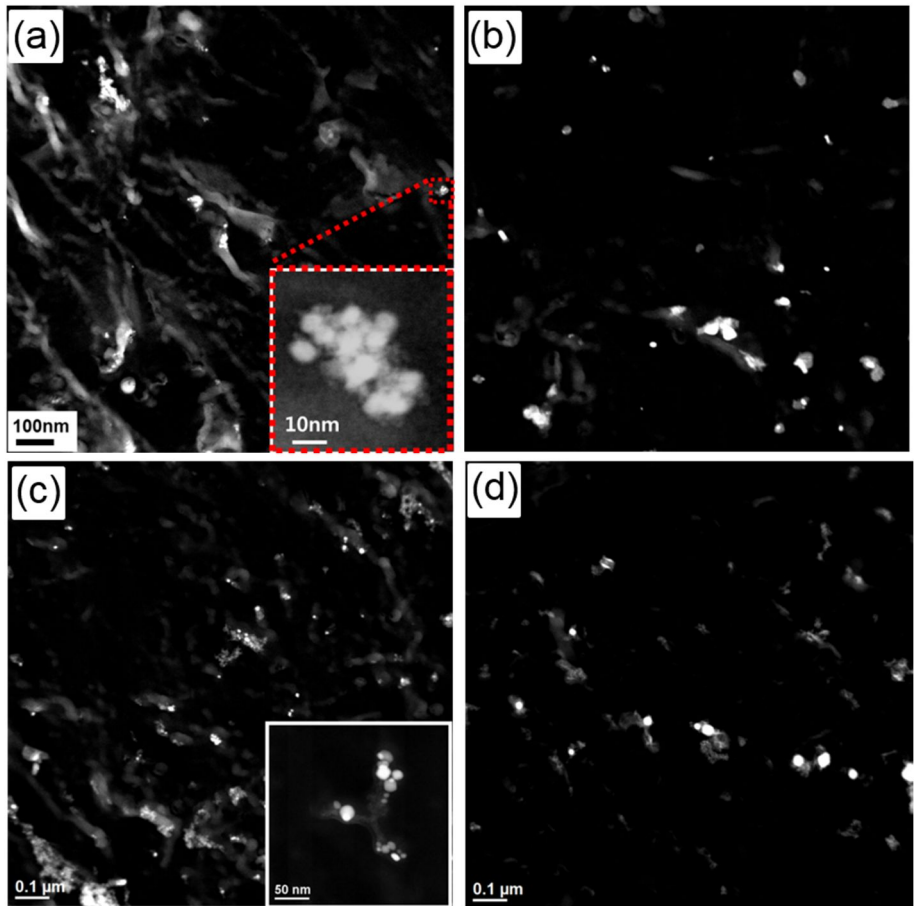


Figure 4.

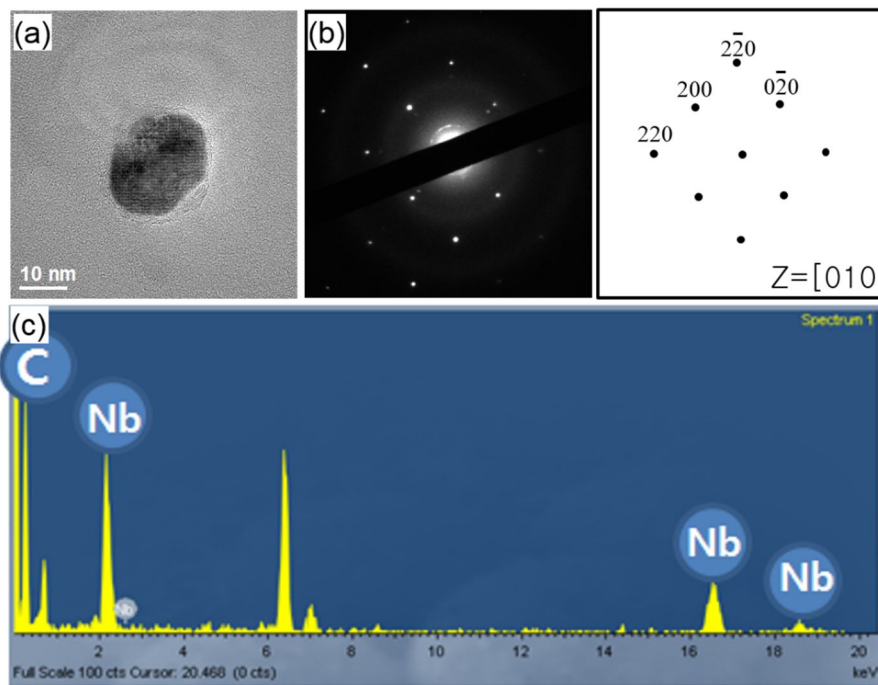


Figure 5.

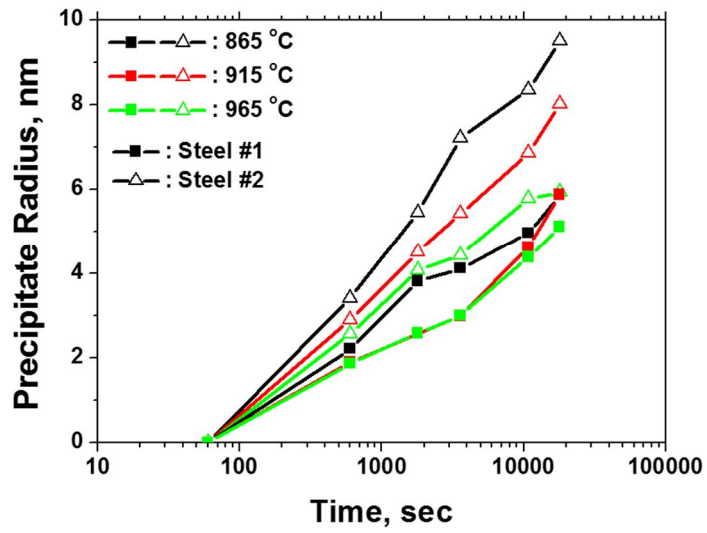
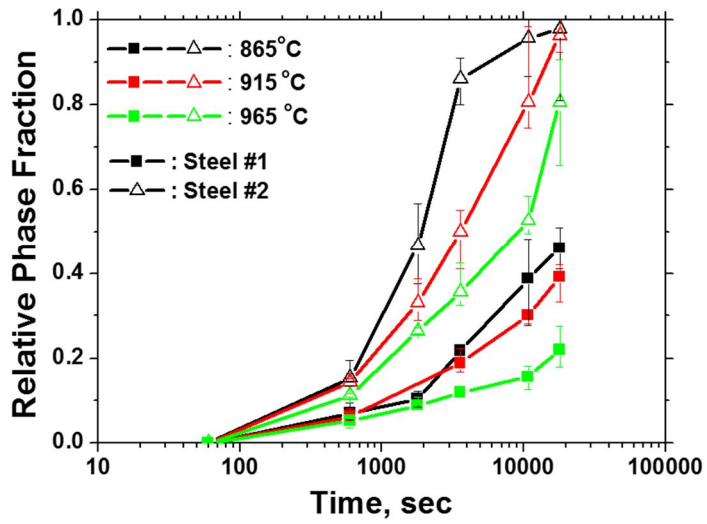


Figure 6.

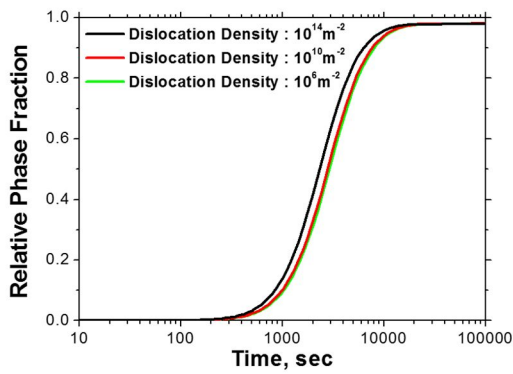
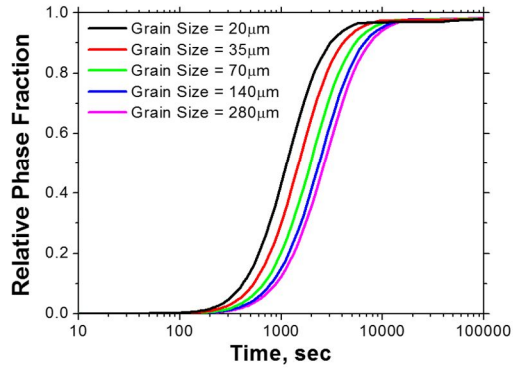
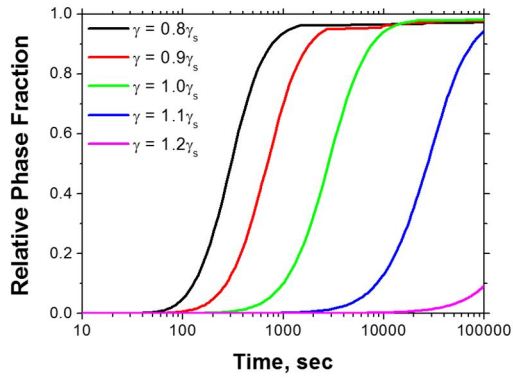


Figure 7.

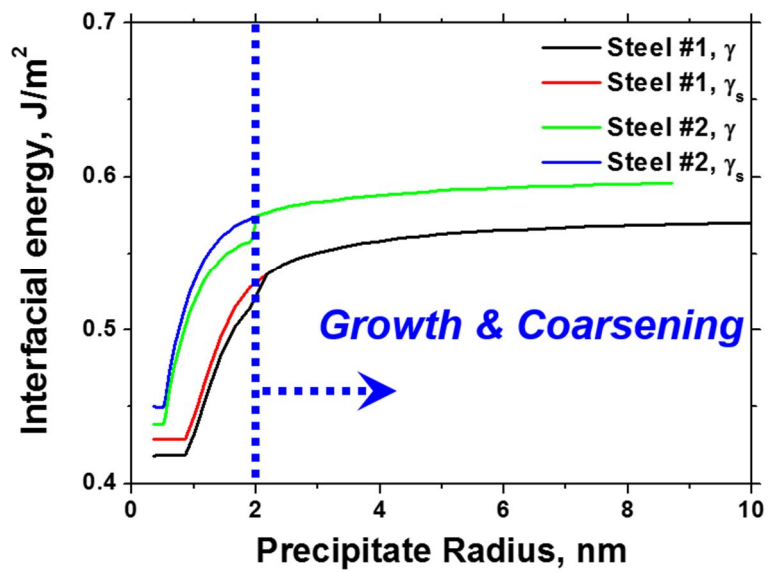


Figure 8.

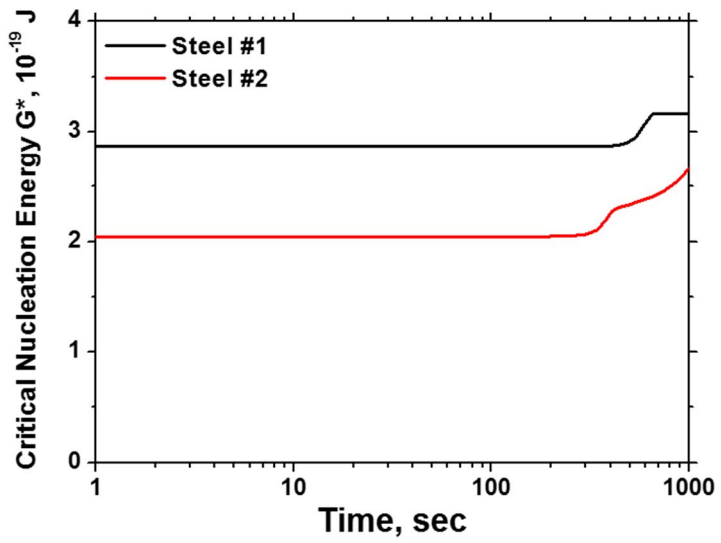
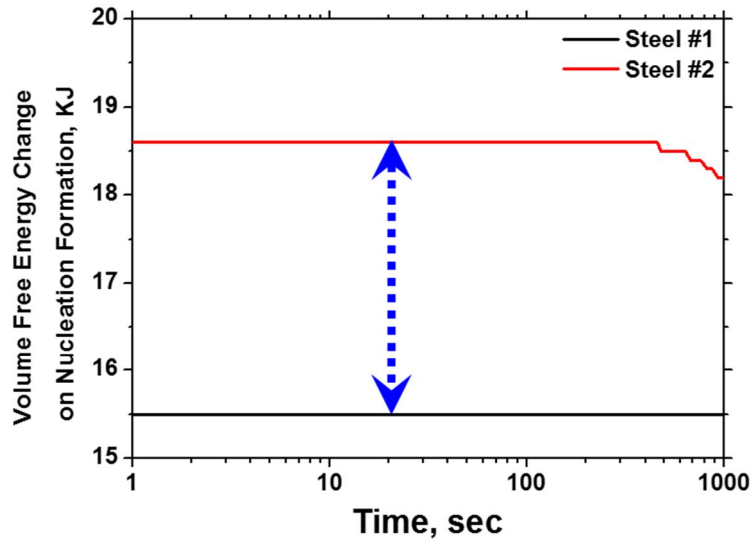


Figure 9.

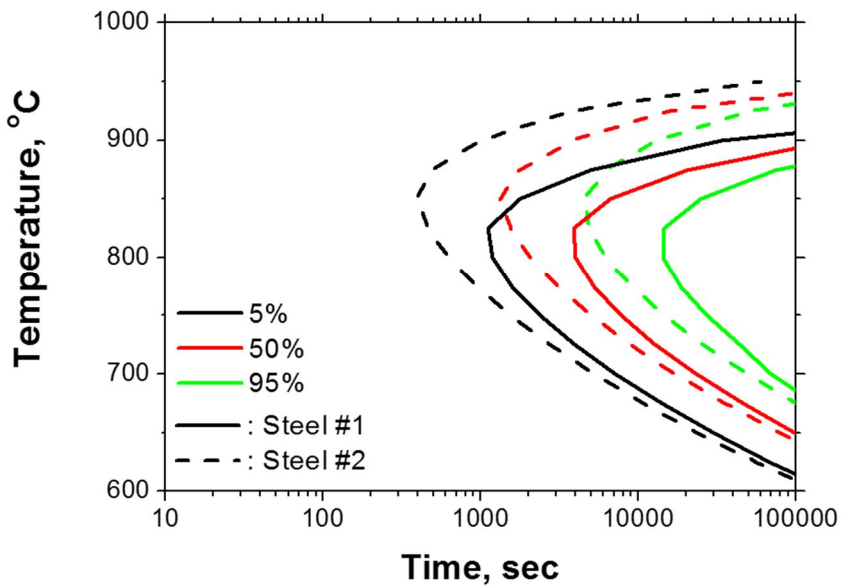
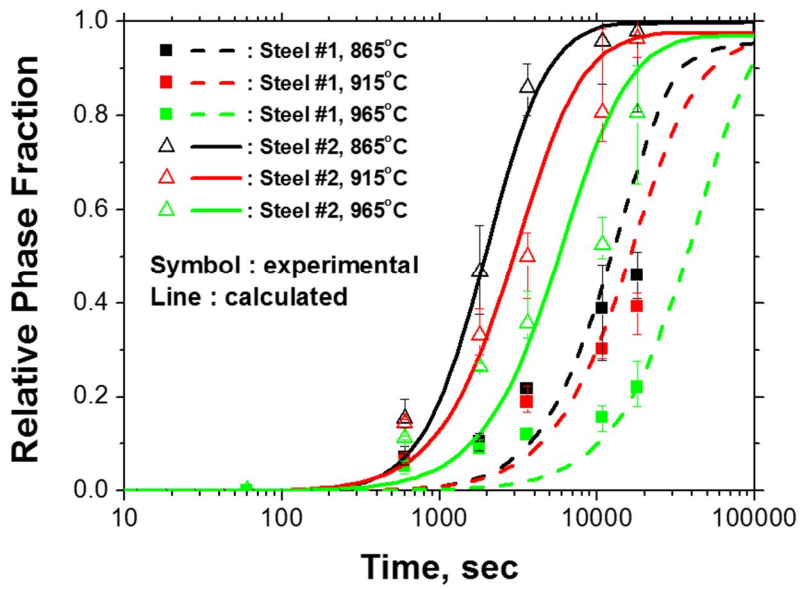


Figure 10.

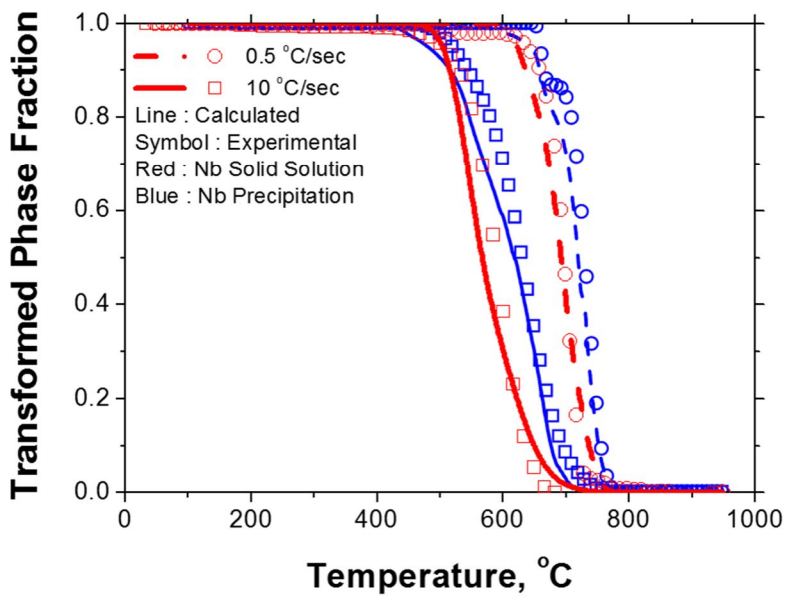
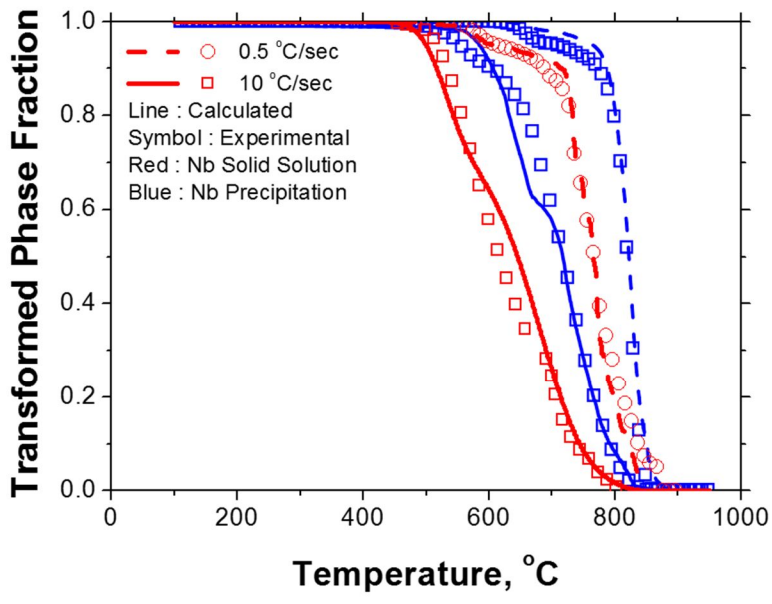


Figure 11.

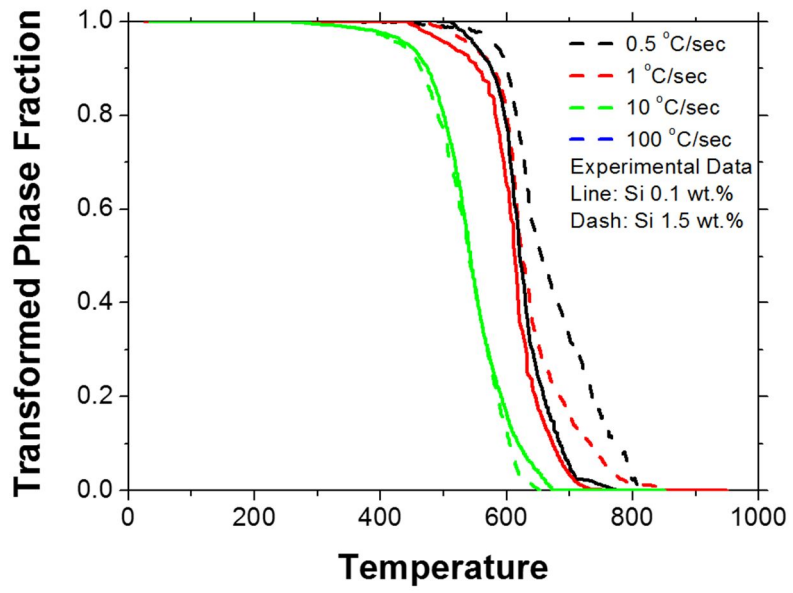


Figure 12.

3.5 Conclusion

In this study, the precipitation behaviors of Nb in the austenite region are measured by TEM observation. The precipitation behaviors are accelerated with addition of Si and the fastest at 865 °C. Using the precipitation model based on KWN and GBB model, we predict various precipitation behaviors and determine appropriate interfacial energy between matrix and precipitate using size correction expression. Phase transformation model combined with Nb precipitation kinetics is modeled based on Johnson–Mehl–Avrami–Kolmogorov equation modified to reflect Nb solid solution and precipitation. Using this modified model and dilatometric analysis, effect of precipitated Nb which accelerates phase transformation is determined.

3.6 References

- [1] A.J. Craven, K. He, L.A. Garvie and T.N. Baker, *Acta Mater.* 48, 3857–68 (2000)
- [2] S.S Campos, E.V. Morales and H.J. Kestenbach, *Metall. Mater. Trans. A.* 32A, 1245–48 (2001)
- [3] M. Charleux, W.J. Poole, M. Militzer and A. Deschamps, *Metall. Mater. Trans. A.* 32A, 1635–47 (2001)
- [4] J.M. Silcock, *ISIJ* 211, 792–800 (1973)
- [5] J.C. Herman, B. Donnay and V. Leroy, *ISIJ Int.* 32, 779–85 (1992)
- [6] I. Weiss and J.J. Jonas, *Metall. Trans. A* 11A, 403–10 (1980)
- [7] S.G. Hong, K.B. Kang and C.G. Park, *Scripta Mater.* 46, 163–68 (2002)
- [8] M. Gomez, S.F. Medina and P. Valles, *ISIJ Int.* 45, 1711–20 (2005)
- [9] J.S. Park, Y.S. Ha, S.J. Lee and Y.-K. Lee, *Metall. Mater. Trans. A* 40A, 560–568 (2009)
- [10] P. Fratzl, O. Penrose and J.L. Lebowitz, *J. Stat. Phys.* 95, 1429 (1999)
- [11] L. Onsager, *Phys. Rev.* 37,405 (1937)
- [12] J. Svoboda, F.D. Fischer, P. Fratzl and E. Kozeschnik, *Mater. Sci. Eng.* A 385,166–74 (2004)
- [13] E. Kozeschnik, J. Svoboda, P. Fratzl and F.D. Fischer, *Mater. Sci. Eng.* A 385,157–65 (2004)

- [14] M.Takahashi and H.K.D.H. Bhadeshia, *J. Mater. Sci. Lett.* 8, 477-478 (1989)
- [15] C.-S. Oh, H.N. Han, C.G. Lee, T.-H. Lee and S.-J. Kim, *Met. Mater.* 10, 399-406 (2004)
- [16] H.N. Han, J.K. Lee, S-H. Park and K.J. Lee, *J. Kor. Inst. Met. Mater.* 38, 409-413 (2000)
- [17] ASTM STP A 1033-04, ASTM International, ASTM, Philadelphia, PA
- [18] T.A. Kop, J. Sietsma and S. van der Zwaag, *J. Mater. Sci.* 36, 519-26 (2001).
- [19] D.-W. Suh, C.-S. Oh, H.N Han and S.-J. Kim, *Acta Mater.* 55, 2659-69 (2007)
- [20] D.-W. Suh, C-S. Oh, H.N. Han and S.-J. Kim, *Metall. Mater. Trans. A* 38A, 2963-73 (2007)
- [21] Y.-G. Cho, D.-W. Suh, J.K. Lee and H.N. Han, *Scripta Mater.* 65, 569-72 (2011)
- [22] R. Kampmann and R. Wagner, *Mater. Sci. Tech.* 5 (1991)
- [23] K Russel, *Adv. Colloid Sci.* 13, 205-318 (1980)
- [24] FK. LeGoues and HI. Aaronson, *Acta Metall.* 32, 1855 (1997)
- [25] B. Sonderegger and E. Kozeschnik, *Metall. Mater. Trans. A* 40, 499-510 (2009)
- [26] W.L. Bragg and E.J. Williams, *Proc. R. Coc.* 145, 699-730 (1934)
- [27] B. Sonderegger and E. Kozeschnik, *Scripta Mater.* 60, 635-38 (2009)

- [28] W.A. Johnson and R.F. Mehl, Trans. AIME. 41, 273-78 (1937)
- [29] H.N. Han and S.-H. Park, Mater. Sci. Technol. 17, 721-26 (2001)
- [30] E. Sheil, Archiv. fuer Eisenhuettenwesen. 8, 565 (1935)

Chapter 4

A finite element simulation for carburizing heat treatment of automotive gear ring incorporating transformation plasticity

4.1 Introduction

The recent tendency in manufacturing the automotive components is to increase their performance while reducing the costs for materials and processing. The surface hardening of carbon steel due to carburizing heat treatment is one of the useful methods to achieve this goal [1,2]. The carburizing heat treatment is one of the thermo-chemical treatments inducing carbon diffusion in steel surface, resulting in the martensite formation during the subsequent quenching [3,4]. The formation of hard superficial layer leads to increase the wear and fatigue properties due to the hardening with a compressive state on the surface [5-9].

However, unfortunately, the carburizing heat treatments often cause excessive and uncontrolled distortion [7-9]. The decreasing trend of the distortion has been a major issue in all the heat treatment processes including carburizing for many years. Many researches have reported various causes of the distortion and found that the phase transformation as well as thermal

expansion/contraction during heat treatment plays an important role [10-12]. In particular, it is known that the transformation plasticity attributed to an anomalous permanent deformation induced by the phase transformation mainly causes unexpected dimensional instability and difficulties in the process optimization [13,14].

The description for the transformation plasticity can be classified into three main groups according to their mechanisms: (1) the weaker phase yielding [15], (2) the favorable variant selection [16,17], and (3) the accelerated diffusion on the migrating transformation interface [18]. First of these mechanisms explains the macroscopic plasticity induced by the volume mismatch between hard and soft phases, which produces the microscopic plasticity in the weaker phase. Several researchers proposed several modified models based on empirical evidences such as the proportionality of the permanent strain to the applied stress and the difference of lattice volumes between the two phases [19,20]. Second important mechanism accounts the anisotropy of the transformation strain during the displacive transformation [16,21,22]. Some of the authors modeled the anisotropic transformation strain based on the selectivity of some specific variants increased by the externally applied stress during the displacive transformation. Another microstructural theory for transformation strain is based on the diffusion mechanism of the migrating interface during the diffusional phase transformation, which can be described as an accelerated Coble creep [13,18,23]. Some of the authors

derived a constitutive equation for the transformation plasticity as a thermally activated form by considering an atomic flux along the phase interface.

Significant efforts have been focused to simulate the realistic industrial problems such as welding and heat treatment by the finite element method (FEM) including the transformation plasticity [14, 24-26]. In particular, because the carburizing heat treatment is closely involved in the metallurgical responses of carbon diffusion and phase transformation as well as the thermo-mechanical response, the multiphysical approach incorporating complex nonlinear thermo-mechanical constitutive equations should be necessary to accurately predict the material behavior during the process [24]. For solving these, the FEM could become one of the most efficient tools due to the recent progress of computing power.

In this study, the carbon diffusion in automotive annulus gear ring, which was made of a medium carbon steel, was solved by the FEM based on Fick's law under the assumption of a constant carbon potential for the entire surfaces of the gear [27,28]. Since the profiles of carbon concentration in the gear strongly affect the phase transformation kinetics, the calculated carbon content after the carburizing was the input data for thermo-mechanical analysis during the subsequent quenching. The parameters adapted in the phase transformation and volume changes were empirically derived as the functions of chemical compositions, temperature and grain size [14,25]. The transformation kinetics of the austenitic phase on cooling was selectively

chosen from the Johnson–Mehl–Avrami–Kolmogorov (JMAK) equation for the diffusional transformation [29-31], whereas Koistinen and Marburger equation was used for the diffusionless martensitic transformation to describe the evolution of phases during the relatively rapid cooling [32]. To extend the JMAK equation under the nonisothermal condition, the concept of additivity rule was introduced under the assumption that the cooling curve can be divided into small time intervals within which the kinetics values remain constant [33,34]. The transformation plasticity for both the diffusional and diffusionless transformations was considered by the constitutive equations corresponding to each transformation mechanism. The constitutive equations for the transformation plasticity were incorporated into the finite element model. Besides the transformation plasticity, an implicit numerical solution procedure to calculate the thermo-elasto-plastic deformation of each constituent phase was implemented into the general purpose implicit finite element program. To validate the suggested FE model, an automotive annulus gear ring was used as the workpiece for the experiments as shown in Fig. 1. The prediction accuracy of the phase evolution, hardness distribution, and dimensional change of the gear ring were verified with the measurement data. The effect of transformation plasticity on the dimensional change was described by the developed numerical model.

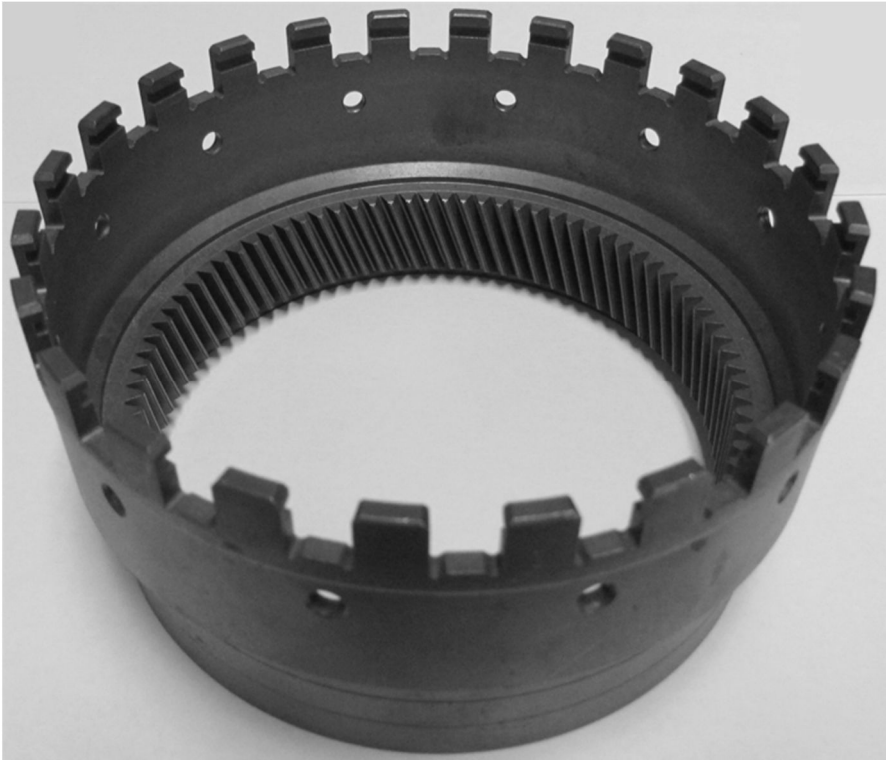


Figure 1.

4.2 Experimental procedure

The automotive annulus gear ring shown in Fig. 1 has 73 teeth, and the diameters of the inner and outer surface were 144 and 147 mm, respectively. It was made of SCR420 steel that has the chemical composition of Fe-0.22wt%C-0.26wt%Si-0.85wt%Mn-1.26wt%Cr. Besides SCR420 steel, a higher carbon steel (S50C) with Fe-0.51wt%C-0.20wt%Si-0.87wt%Mn-1.20wt%Cr was prepared to investigate the effect of carburizing heat treatment on the phase transformation kinetics.

In this study, two vacuum carburizing conditions in a continuous furnace were adapted as shown in Figs. 2a and b. In the first condition (case 1), the temperature for carburizing and diffusing is 930 °C, and the gear was cooled down to 830 °C and hold for 20 min. In the second one (case 2), the lower temperatures of 800 and 750 °C for carburizing/diffusing and holding were applied. The process times for carburizing and diffusing were 70 and 160 min, respectively. The carbon concentration of the furnace atmosphere was 1.0 wt% during the carburizing, and this was changed to 0.8 wt% during the following diffusing process. After the vacuum carburizing treatment, the gear was oil-quenched to room temperature.

After the vacuum carburizing heat treatment, the carbon concentration in the gear was measured using a glow discharge spectrometer (GDS, LECO

GDS-850A), an elemental depth profiler. The copper anode had a diameter of 4 mm, and the glow discharge lamp was applied to the sample under a DC voltage of 700 V and a plasma current of 20 mA. The microstructures of the gear ring were observed using an optical microscope, (OM, Olympus GX51) and electron backscatter diffraction (EBSD, TSL OIMTM). The samples were prepared by the standard metallographic grinding procedure followed by chemical etching with a solution of 3% nitric acid–97% ethyl alcohol solution and electropolishing with a solution of 20% perchloric acid–80% ethanol for the OM and EBSD measurement, respectively. The hardnesses on various regions in the gear were measured using a micro-Vickers hardness tester (AKASHI, MVK-H2) with a load and dwell time of 4.9 N and 10 s, respectively.

To evaluate the parameters in JMAK equation for the phase transformation from austenite during cooling, we used the dilatometric measurement performed using a transformation dilatometer (R&B, TM-111129-001). Two type specimens of SCR420 (0.22 wt% C) and S50C (0.51 wt% C) were prepared to compare the effect of the carbon content on the phase transformation. The specimens were heated by an induction coil in a vacuum to 950 °C at a heating rate of 10 °C/s, then austenitized for 5 min, followed by cooling to room temperature at various cooling rates of 1, 2, 10, 20, and 40 °C/s.

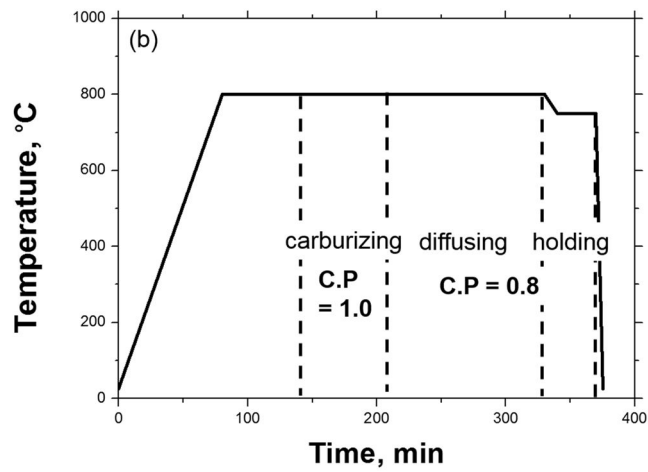
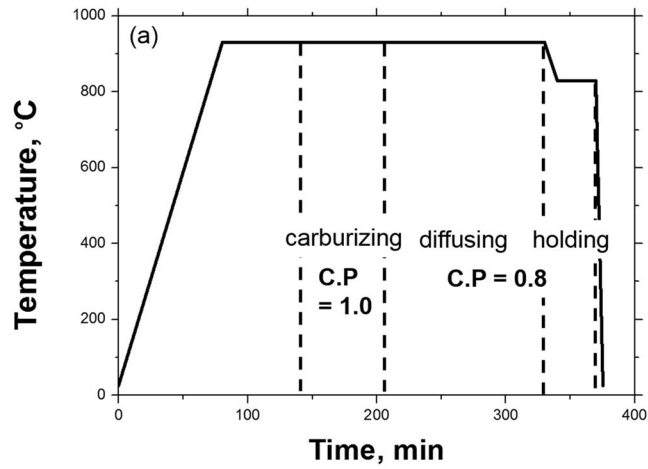


Figure 2.

4.3 Model developemnet

Since the carburizing heat treatment is a complex multiphysics problem, the rigorous treatment for the problem requires a thermo-mechanical calculation incorporating the phase transformation model as well as the carbon diffusion model. The representation of the physical models and coupling considered for the carburizing heat treatment is shown in Fig. 3. Each physical model is explained as follows.

4.3.1 Phase transformation model

Ferrite/pearlite-to-austenite and austenite-to-ferrite/pearlite/bainite transformations have been defined as the diffusional precipitation reaction, and the transformed phase fraction, X , during the isothermal austenite decomposition was derived by using the JMAK type equation:

$$X = 1 - \exp(-kt^n) \quad (1)$$

where t is the total time for transformation at a given temperature. The rate constant k depends on the temperature and transformation mechanism, and the time exponent n is a constant over the temperature range when a unique

transformation mechanism only operates.

In order to extend the above JMAK equation for the phase transformation under the nonisothermal condition, the concept of additivity rule based on the theory of Scheil, was introduced under the assumption that the cooling curve can be divided into small time intervals within which the kinetics values remain constant [33]. The transformed phase fraction until the i -th step, X_i , is expressed as follows:

$$X_i = 1 - \exp\left(-X_{i-1}^{ex} + \Delta X_i^{ex}\right), \quad \Delta X_i^{ex} = nk_i t_i'^{n-1} \Delta t, \quad t_i' = \left(\frac{X_{i-1}^{ex}}{k_i}\right) \quad (2)$$

where t' is the equivalent transformation time needed to transform into the extended fraction of X_{i-1}^{ex} at the temperature of the i -th step, and Δt is the time step corresponding to the i -th step. The values k and n were determined from the dilatation data obtained by the continuous cooling tests using an inverse additivity technique [34]. The initial microstructure of the gear is assumed to be ferrite and pearlite, and the k and n values for ferrite/pearlite to austenite transformation during the heating stage and for austenite to ferrite/pearlite/bainite transformations during the quenching stage are listed on Table 1, respectively. In the table, the k and n values are a function of chemical composition, austenite grain size, and temperature. C_A (wt%), Ae_3 ,

and Ae_I are the weight percentage of carbon in untransformed austenite and the equilibrium transformation temperatures, respectively. Those values were calculated by thermodynamic analysis using Thermo-Calc software under para equilibrium [35,36]. B_s , AGS (μm), and T are the bainite start temperature based on Zhao's empirical equation [37], prior austenite grain size, and temperature in Celcius, respectively. The diffusivity of carbon in the austenite matrix, D_c , was used as a function of temperature and carbon content [38].

$$D_c = 4.53 \times 10^{-7} \left\{ 1 + C_A (100 - C_A) \frac{0.19}{T} \right\} \exp \left\{ - \left(\frac{1}{T} - 2.22 \times 10^{-4} \right) (17767 - 57.67 C_A) \right\} \quad (3)$$

For the diffusionless phase transformation, which only depends on temperature, it is known that the athermal martensitic transformation during cooling can be well described as the Koistinen and Marburger's empirical equation [32]:

$$\frac{X_M}{1 - X_F - X_P - X_B} = 1 - \exp[-0.011(M_s - T)] \quad (4)$$

where M_s is the martensite start temperature affected by the carbon content in austenite [39]; the subscripts F , P , B , and M are for ferrite, pearlite, bainite, and martensite, respectively.

4.3.2 Carburizing model

The carbon potential on the surface depends on the temperature and the pressure. It remains constant during the treatment and at the same time the carbon diffuses into the material. Based on the temperature- and pressure-driven diffusion, the flux of carbon concentration in steel, J , can be derived by Fick's law as follows [40]:

$$J = -sD_c \cdot \left[\frac{\partial \Phi}{\partial x} + \kappa_s \frac{\partial}{\partial x} [\ln(T + 273)] + \kappa_p \frac{\partial p}{\partial x} \right] \text{ and } \Phi = \frac{c}{s} \quad (5)$$

where D_c , Φ , c , p , and s are the carbon diffusivity mentioned in Eq. (3), activity of the diffusing carbon, mass concentration of carbon, pressure on the surface, and carbon solubility obtained from the thermodynamic analysis by Thermo-Calc, respectively. The temperature- and the pressure-driven diffusion can be expressed by the following equations.

$$\kappa_s = \frac{c(T + 273)}{s^2} \frac{\partial s}{\partial T} \text{ and } \kappa_p = \frac{c}{s^2} \frac{\partial s}{\partial p} \quad (6)$$

where κ_s is the Sorret effect factor representing the relationship between diffusion and temperature, and κ_p is the pressure factor representing the extent of diffusion with respect to the surface pressure.

The dissociated carbon atoms from the carburizing gas were delivered to the gear surface as a flux, J_s . The boundary condition was determined by Eq. (7) across the surface layer.

$$J_s = \beta(C_f - C_s) \quad (7)$$

where β is the coefficient of surface reaction rate and was obtained as 1.4×10^{-7} m/s at 930 °C and 0.7×10^{-7} m/s at 750 °C [7]. The linear interpolation between 750 and 930 °C was used to obtain the value in-between temperature. The C_f and C_s indicate the carbon potential of the furnace atmosphere and carbon content in the steel surface, respectively.

4.3.3. Transformation plasticity model

In this study, the transformation plasticity model proposed by Han *et. al* was adopted to explain the mechanism of diffusional phase transformation [18]. According to this theory, when a stress is applied during the phase transformation, the migrating atoms move to release the applied stress field,

inducing an atomic flux along the phase interface. Using this concept, a constitutive equation for the diffusional transformation plasticity was described as a function of the transformation rate (\dot{X}) and applied stress (σ):

$$\dot{\varepsilon}^{TP} = \frac{1}{3} \frac{d_0}{\delta} \dot{X} \frac{\sigma \Omega}{k_B T} c_{v0} \exp\left(-\frac{Q_f}{k_B T}\right) \quad (8)$$

where d_0 is the initial grain size of the parent phase, δ is the effective thickness of the interface, Ω is the volume of the vacancy, c_{v0} is a dimensionless constant determined by the change in thermal entropy associated with the formation of vacancies, and Q_f is the formation enthalpy of the vacancy at the interface. The Boltzmann constant, k_B , has a value of 1.38×10^{-23} J/K. In this study, the initial grain size of the austenite phase was measured as 30 μm . Ω , δ , Q_f , and c_{v0} were 1.21×10^{-29} m^3 [41], 1 nm, 80 kJ/mol, and 1.2 [18], respectively.

In the diffusionless transformation, the anisotropic transformation strain is caused by the selectivity of some specific variants increased by the externally applied stress [21]. It was reported that the transformation strain increases almost linearly as the applied stress. Therefore, in order to explain the transformation plasticity during the martensite transformation, the linear

model was adopted as follows:

$$\dot{\varepsilon}^{TP} = A\dot{X}\sigma \quad (9)$$

where the constant A was experimentally obtained as $2 \times 10^{-10} \text{ Pa}^{-1}$ [16].

4.3.4. Heat transfer model

The temperature field of the gear during the carburizing heat treatment was calculated considering a latent heat generated due to the phase transformation. The heat transfer equation is listed in the following form:

$$\rho C_p \dot{T} = \nabla \cdot (k_t \nabla T) + \Delta H_F \cdot \dot{X}_F + \Delta H_P \cdot \dot{X}_P + \Delta H_B \cdot \dot{X}_B + \Delta H_M \cdot \dot{X}_M \quad (10)$$

where ρ and k_t are the density and thermal conductivity, respectively. The density of the steel is listed in Table 2 as a function of alloying element and temperature [42]. In the Table 2, C_A and C_F are the carbon content in untransformed austenite which can be calculated from the mass balance of carbon in the austenite and transformed phases, and the solute carbon content in ferrite which is assumed as an equilibrium value calculated by the

thermodynamic calculation. In this study, the density of pearlite was calculated by the mixture of ferrite and cementite densities, and the phase fraction of cementite was obtained by the lever rule considering the carbon concentration. The densities of bainite and martensite were assumed as that of ferrite, because the difference among the ferrite, bainite, and martensite densities is negligible. The density of phase mixture can be determined from the mixture rule. The temperature dependent isotropic conductivity is also listed in Table 3 [43]. As shown at Fig. 4, C_p and ΔH are the temperature dependent heat capacity and heat evolution due to the phase transformation, respectively, and these parameters were calculated by thermodynamic analysis. The heat evolved from the ferrite formation (ΔH_F) was obtained by the reaction, $\gamma \rightarrow \gamma' + \alpha$ divided by the mole fraction of the ferrite formed. The heat evolved from the pearlite formation (ΔH_P) is the heat of reaction, $\gamma \rightarrow \alpha + cm$. For the formation of bainite, an additional shear energy of 600 J/mol was considered to achieve the phase equilibria [44]. The heat evolved from the bainite formation (ΔH_B) is obtained by the reaction $\gamma \rightarrow \alpha - 600$ J/mol. The heat evolved from the martensite formation (ΔH_M) was determined by the following equation [16]:

$$\Delta H_M = -2100 + \left(\frac{2100}{T_0 - M_s} \right) \cdot (T - M_s) \quad (11)$$

where T_0 is the temperature at which the difference of Gibbs free energy between austenite and martensite is zero.

The boundary condition of the heat transfer on the outer surface was assumed to be

$$\Psi = h(T_f - T_s) \quad (12)$$

where T_f , T_s , Ψ , and h are the furnace temperature, surface temperature of the gear, heat flux, and heat transfer coefficient, respectively. The history of furnace temperature is shown in Fig. 2, and the heat treatment coefficient between the gear surface and furnace atmosphere is $3000 \text{ W/m}^2 \cdot ^\circ\text{C}$ [9]. During the quenching process, the furnace temperature was assumed as $25 \text{ }^\circ\text{C}$, and the temperature dependent heat transfer coefficient between the gear surface and coolant oil was used as $300 \sim 2500 \text{ W/m}^2 \cdot ^\circ\text{C}$ considering the temperature of the gear surface [7].

4.3.5 Constitutive equations

The stress increment of the Cauchy stress ($d\sigma$) is

$$d\boldsymbol{\sigma} = \mathbf{C}^e : d\boldsymbol{\varepsilon}^e \quad (13)$$

where \mathbf{C}^e and $d\boldsymbol{\varepsilon}^e$ are the elastic stiffness tensor and elastic strain increment, respectively. The total strain increment ($d\boldsymbol{\varepsilon}^T$) is

$$d\boldsymbol{\varepsilon}^T = d\boldsymbol{\varepsilon}^e + d\boldsymbol{\varepsilon}^p + d\boldsymbol{\varepsilon}^v + d\boldsymbol{\varepsilon}^{TP} \quad (14)$$

where $d\boldsymbol{\varepsilon}^v$, $d\boldsymbol{\varepsilon}^{TP}$, and $d\boldsymbol{\varepsilon}^p$ are the volumetric strain increment due to the phase transformation and temperature change, the transformation plasticity (TP) strain increment associated with both the diffusional and displacive phase transformations, and the plastic strain increment, respectively [45].

For the volumetric strain ($d\boldsymbol{\varepsilon}^v$), the linear mixture of the strain increments of the existing phases was assumed as follows:

$$d\boldsymbol{\varepsilon}^v = \sum X_i d\boldsymbol{\varepsilon}_i^v = \sum X_i \cdot \left(\frac{1}{3} \frac{\rho_i}{d\rho_i} \right) \mathbf{I} \quad (15)$$

where X_i is the phase fraction of each phase predicted by the phase transformation model, ρ_i is the density of each phase listed in Table.2, and \mathbf{I} is the identity tensor.

The flow stress curves based on Misaka's equation were used to

describe the mechanical behavior of the material related to the change in the carbon concentration [46]:

$$\sigma = \exp\left(0.126 - 1.75 \cdot C + 0.594 \cdot C^2 + \frac{2851 - 2968 \cdot C - 1120 \cdot C^2}{T}\right) \cdot (\varepsilon^p)^{0.21} \cdot (\dot{\varepsilon}^p)^{0.13} \quad (16)$$

where σ , C , T , ε^p , and $\dot{\varepsilon}^p$ are the stress, carbon concentration in weight percentage, temperature, plastic strain, and plastic strain rate, respectively. This flow stress curves and the transformation plasticity strain based on Eqs. (8) and (9) are implemented into the FE code.

These strain increments were obtained from the above equations, and consequently, the stress increment becomes:

$$d\sigma = \mathbf{C}^e : (d\varepsilon^T - d\varepsilon^v - d\varepsilon^{TP} - d\varepsilon^p) \quad (17)$$

The temperature dependent isotropic elastic modulus was used to obtain the elastic stiffness of carbon steel, as listed in Table 3 [43]. The Poisson's ratio of the steel is also listed in Table 3 over the temperature range.

Table 1. The values of k and n from JMAK equation for various phase transformations.

	$\ln(k)$	n
Ferrite to austenite	$-1.11 + \ln(Ae_1 - T) - \frac{47426}{T}$	$0.248 \cdot (1 - X_\gamma)^{0.195}$
Pearlite to austenite	$0.33 + \ln(Ae_1 - 30 - T) - \frac{155436}{T}$	$0.195 \cdot (1 - X_\gamma)^{0.026}$
Austenite to ferrite	$4.45 - 0.75 \cdot \ln(AGS) + (2.60 - 0.29C_A) \cdot \ln(D_c)$ $+ \left(-2.61 + 5.09C_A^{0.38} + 1.55C_A^2\right) \cdot \ln\left(\frac{Ae_3 - T}{Ae_3}\right)$ $+ 19.03 \cdot \ln\left[\sin\left\{\frac{2\pi \cdot (T + 273)}{4(Ae_3 - 80)}\right\}\right]$	$2.60 - 0.29 \cdot C_A$
Austenite to pearlite	$5.31 + 1.43 \cdot \ln(AGS) + (15.08 - 21.68C_A) \cdot \ln(D_c)$ $+ \left(-3.96 - 0.06C_A^{1.00} - 7.15C_A^2\right) \cdot \ln\left(\frac{Ae_1 - T}{Ae_1}\right)$ $+ 6.50 \cdot \ln\left[\sin\left\{\frac{2\pi \cdot (T + 273)}{4(Ae_1 - 80)}\right\}\right]$	$15.08 - 21.68 \cdot C_A$
Austenite to bainite	$4.29 - 0.04 \cdot \ln(AGS) + (1.63 - 0.03C_A) \cdot \ln(D_c)$ $+ \left(4.13 + 7.68C_A^{1.56} + 1.59C_A^2\right) \cdot \ln\left(\frac{Bs - T}{Bs}\right)$ $- 10.41 \cdot \ln\left[\sin\left\{\frac{2\pi \cdot (T + 273)}{4(Bs - 80)}\right\}\right]$	$1.63 - 0.03 \cdot C_A$

Table 2. Densities of each phases as a function of temperature and chemical composition [42].

Phase	Density (kg/m ³)
Austenite	$8099.79 - 0.5060T + (-118.26 + 0.00739T)C_A - 68.24Si - 6.01Mn$
Ferrite	$7875.96 - 0.2970T - 0.0000562T^2 + (2206.35 + 0.0077T)C_F - 36.86Si - 7.24Mn$
Cementite	$7686.45 - 0.0663T - 0.000312T^2$

Table 3. Elastic modulus, Poisson's ratio and thermal conductivity of steel at various temperatures [43].

T (°C)	E (GPa)	Poisson's ratio	k_t (W/m·°C)
0	210	0.280	50
300	185	0.296	45
600	135	0.310	38
700	100	0.325	33
900	100	0.325	28
1000	100	0.325	28

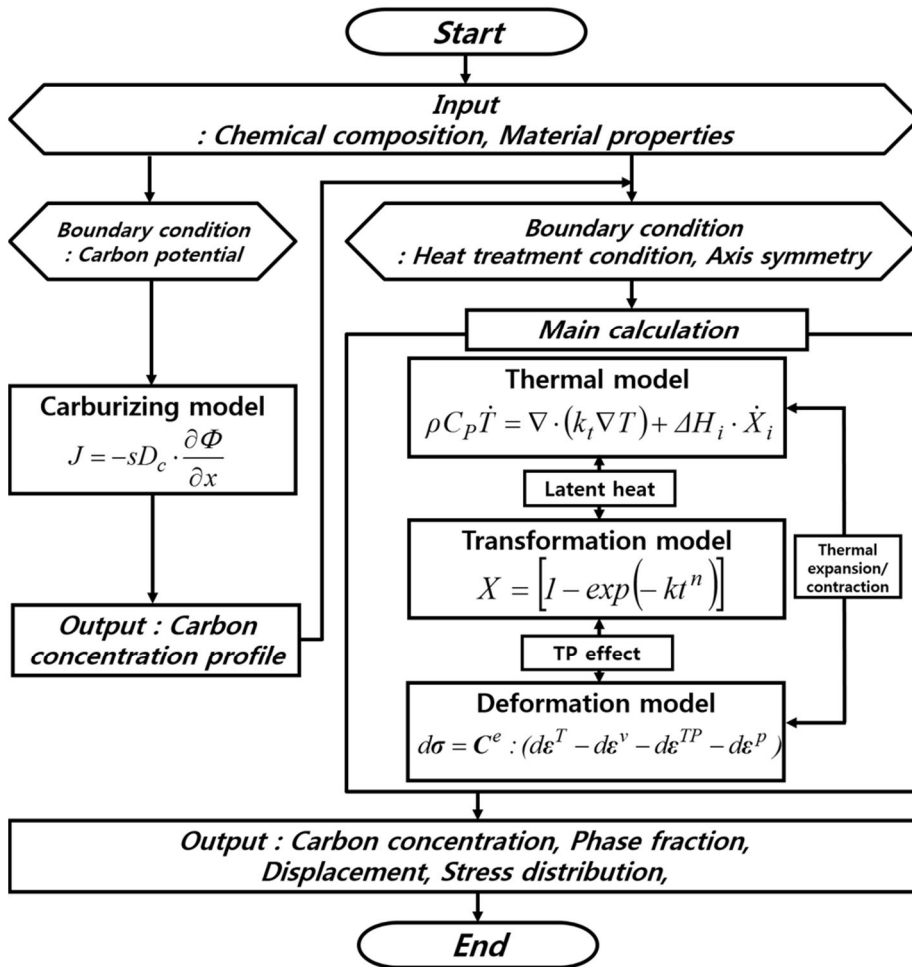


Figure 3.

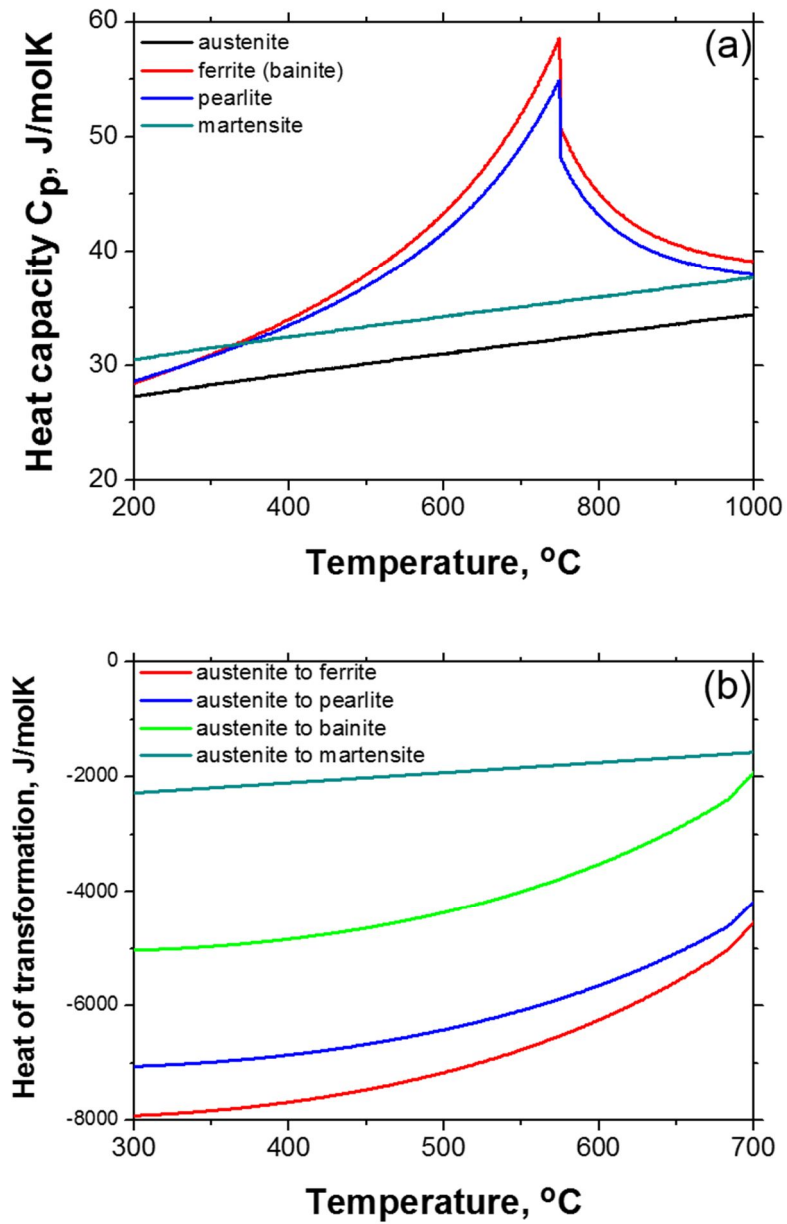


Figure 4.

4.4 Results and discussion

Fig. 5a shows the distribution of the carbon concentration in the gear after the carburizing heat treatment at 930 °C in Fig. 2a (case 1). The carbon concentration at the gear surface is higher than that inside the gear. In particular, the gear tooth has the highest carbon concentration of about 0.8 wt. % due to the relatively large surface area. Fig. 5b shows the comparison between the measured and calculated carbon concentrations at the area indicated by the black square in Fig. 5a. The carbon concentrations after the carburizing heat treatments at 930 °C (case 1) and 800 °C (case 2) are illustrated in red and blue colors, respectively. The symbols and lines indicate the experimental and calculated data, respectively. The carbon profile solved by the finite element simulation based on the temperature- and pressure-driven carbon diffusion agrees well with the experimental data measured using a glow discharge spectrometer. In Fig. 5b, case 2 shows lower carbon concentration at the surface region compared to that in case 1, since the higher carburizing temperature leads to more rapid carbon diffusion. The carburizing depth in case 1 is also deeper than that in case 2, due to the difference of carburizing temperature.

As shown in Fig. 5a, the range of carbon concentration after carburizing is from 0.22 wt% to 0.8 wt%. Two steels with almost same amount of alloying

element except carbon, SCR420 (0.22 wt% C) and S50C (0.51 wt% C), were prepared to investigate the effect of carbon concentration on phase transformation kinetics. Figs. 6 and 7 show the behaviors of the phase transformation and microstructures of SCR420 and S50C under various cooling rates, respectively. The phase transformation kinetics were measured by the dilatometry of the two steels and compared to the phase transformation model described in section 3.1. The symbols and lines indicate the experimental and calculated data, respectively. For 0.22 wt.%C steel, as shown in Fig. 6a, the ferrite/pearlite phase transformation mainly occurs at near 600 ~ 800 °C under the relatively slow cooling rate of 1~2 °C/s, whereas the bainite is formed below 600 °C under the high cooling rate of over 20 °C/s. Below 400 °C, the martensitic transformation is observed. For 0.51 wt.%C steel shown in Fig 7a, the higher carbon concentration significantly delays the ferrite transformation at a slow cooling rate of 1 °C/s and decreases the martensite start temperature down to below 300 °C.

Figs. 6b–e and Figs. 7b–e show the optical microstructure of SCR420 and S50C under various cooling rates, respectively. As shown in Figs. 6b and 7b, the ferrite and pearlite structure are mainly formed in both the steels under a slow cooling rate of 1 °C/s. While, as shown in Figs. 6d and 7d, the bainite and martensite phases are mainly formed under a relatively fast cooling rate of 10 °C/s. The martensite fraction in S50C with higher carbon content is larger than that in SCR420 at the same cooling rate of 10 °C/s. Over cooling rate of

20 °C/s, the single martensite structure are obtained in whole sample. The microstructural results are in good agreement with the developed phase transformation model.

Fig. 8 shows the phase diagram of the base materials with the variation of carbon content calculated from Thermo-Calc software under para equilibrium [35,36]. The holding temperatures after carburizing in cases 1 and 2 are shown in this figure. In case 1, the entire sample could be expected to be single austenite structure at a holding temperature of 830 °C, whereas in case 2, the austenite and the ferrite in the region with below 0.5 wt% carbon might coexist at a holding temperature of 750 °C.

Figs. 9a–d show the optical microstructures at the surface and inner regions in the gear after the carburizing heat treatments. At the gear surface carburized at 930 °C (case 1), the entire sample was observed as almost single martensite structure. As the depth was increased, the ferrite fraction was somewhat increased. It should be noted that in case 2, the ferrite fraction at the inner region significantly increased compared to that in case 1. The increase in the ferrite fraction at the inner region can be described not only by the slower cooling rate and the lower carbon content but also the pre-existing ferrite at a holding temperature of 750 °C. The phase fractions were quantified from the image analysis for the optical and SEM [47] microstructures and compared to the finite element simulation. Fig. 10 shows the comparison between the measured phase fractions and predicted ones. The predicted

results agreed well with the measured data.

Fig. 11 shows the variations in the calculated radial displacement of the gear ring during the carburizing heat treatment (case 1). The calculated region was indicated by a black square in Fig. 5a. The radial displacement shows linear thermal expansion and contraction characteristics in the temperature range where no transformation occurs during the heating and cooling. During the phase transformation, the nonlinear behavior was obtained, because of the atomic volume difference of the FCC and BCC phases [48]. It is interesting that the geometry change along the radial direction considerably increased when the TP strain due to the phase transformation was considered. In Figs. 12a and b, the measured length changes along the radial direction are compared to the finite element simulations in cases 1 and 2, respectively. While the predicted results (red bar) considering the TP strain well matches with the experimental data, the length change (blue bar) was significantly underestimated when the TP strain due to the phase transformation was neglected. It should be noted that the radial length change in case 2 is much smaller than that in case 1. The decrease in the length change in case 2 can be described by decreasing amount of phase transformation due to the preexisting ferrite at a holding temperature of 750 °C, as shown in Fig. 8.

The hardness of the carburized gear, affected by its carbon concentration and phase, is very important criteria to evaluate its performance. Thus, many researchers have developed the method for predicting the

hardness distribution of quench steel based on a linear mixing rule for hardness of each phase as a function of alloying elements and cooling rate. Ion and Anisdahl proposed the hardness equations of each phase as follows [49]:

$$H_F = 42 + 223C_F + 53Si + 30Mn + 12.6Ni + 7Cr + 19Mo + (10 - 19Si + 4Ni + 8Cr + 130V) \log V' \quad (18)$$

$$H_B = -323 + 185C_B + 330Si + 153Mn + 65Ni + 144Cr + 191Mo + (89 + 53C_B - 55Si - 22Mn - 10Ni - 20Cr - 33Mo) \log V' \quad (19)$$

where H_F and H_B are the hardness of ferrite and bainite, respectively, C_F and C_B are the carbon content in ferrite and bainite, and the unit of element used as the weight percentage, and V' is the cooling rate at 700 °C.

The hardness of martensite, H_M , is described as follows [50]:

$$H_M = 3.03 \times 10^{-7} \cdot T_i (37.9 + \ln t_i)^2 - 0.0289 \cdot T_i (37.9 + \ln t_i) + \left[874.9 - 202.2 \cdot \left(\frac{0.22}{C_M} \right)^2 \right] \quad (20)$$

where T_i and t_i are the tempering temperature and time, respectively, and C_M is the carbon content in martensite. In order to consider nonisothermal cooling, Eq. (20) was treated as a combination of a sufficiently large number of

isothermal tempering steps [33].

Finally, the apparent hardness of the gear after carburizing heat treatment was calculated using the above equations and compared to the measured data. Fig. 13 shows the measured and calculated profiles of Vickers hardness as a function of depth. The calculated results agreed well with the measured data. In case 1, the measured hardness is the maximum value of 780 HV at the surface, with the highest carbon concentration. In the center of the gear where the effect of carburizing is negligible, the hardness is the minimum value of 500 HV. This means that the surface region with faster cooling rate and higher carbon concentration is harder than the inner region. As shown in the hardness profile in case 2, the measured hardness at the gear surface and inside are 610 HV and 350 HV, respectively. Compared to the measured hardness of case 1, this result represents relatively lower hardness. This phenomenon could be understood by the lower carbon concentration and remaining ferrite phase at the inner region.

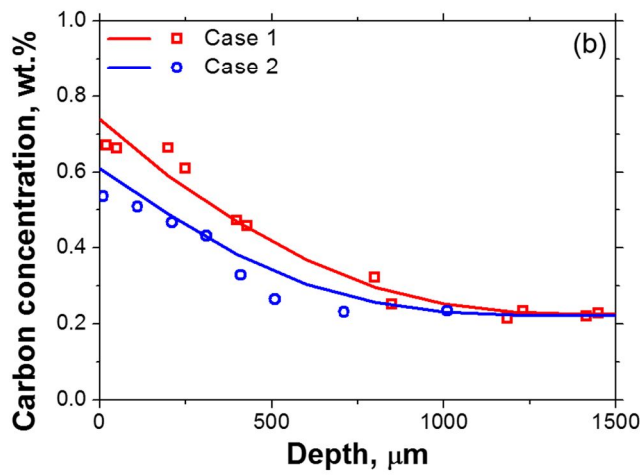
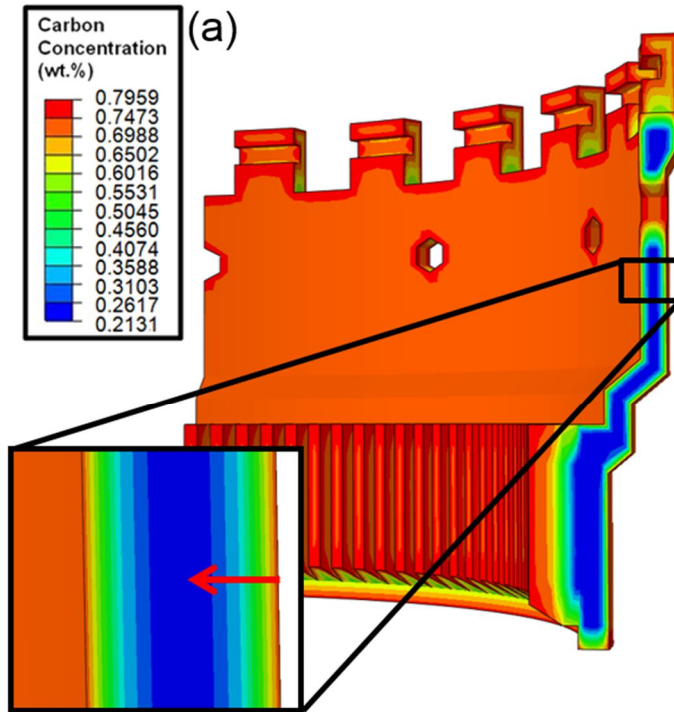


Figure 5.

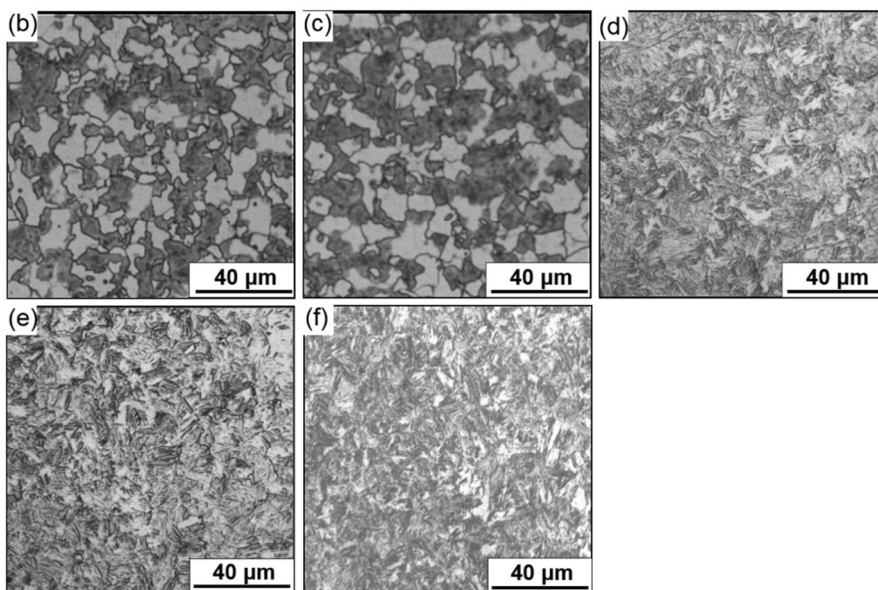
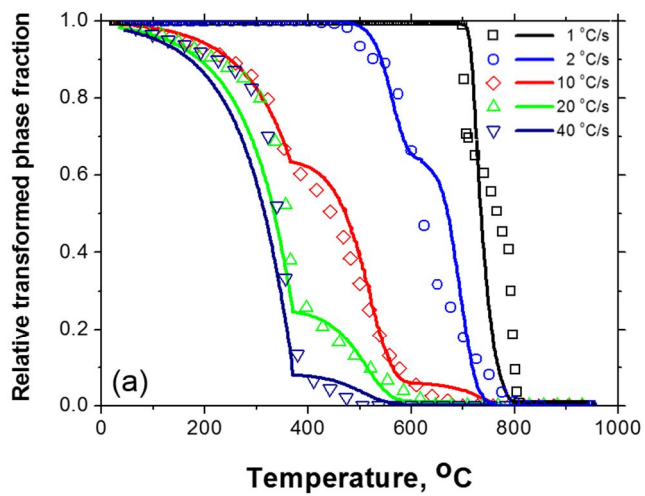


Figure 6.

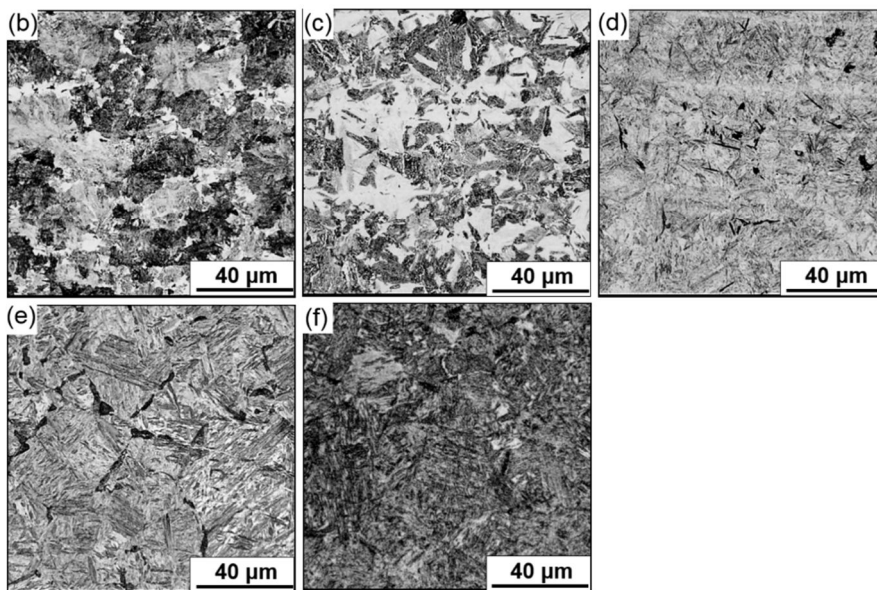
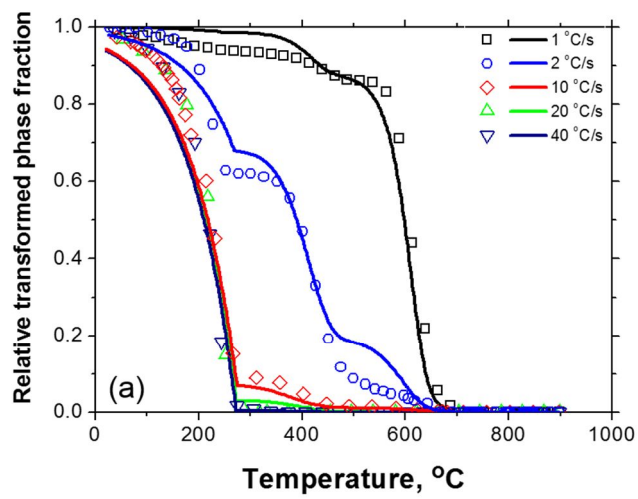


Figure 7.

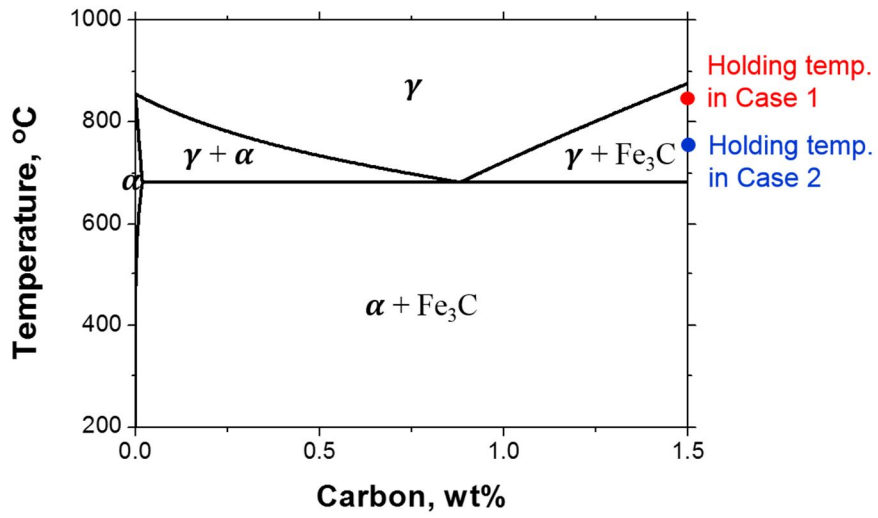


Figure 8.

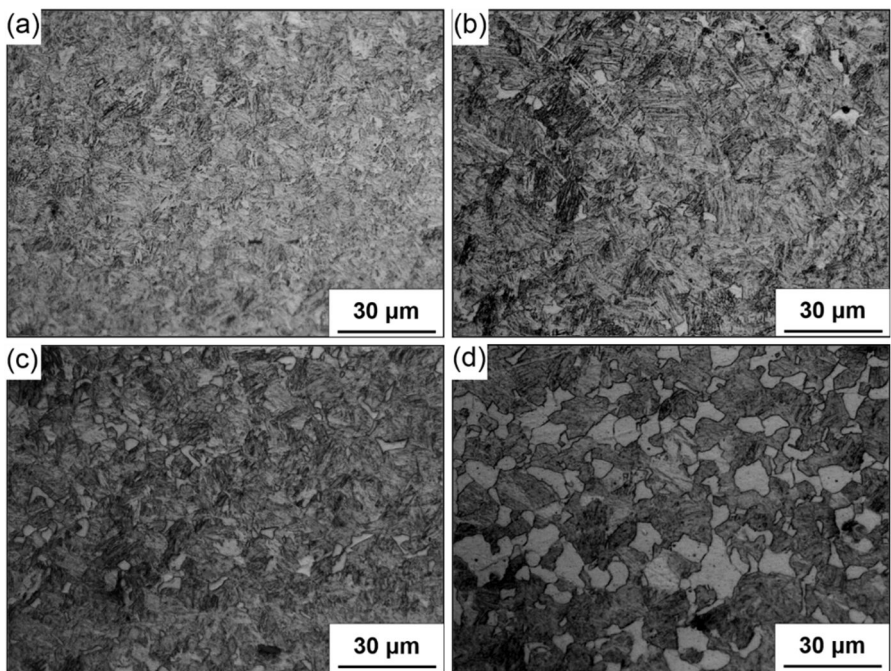


Figure 9.

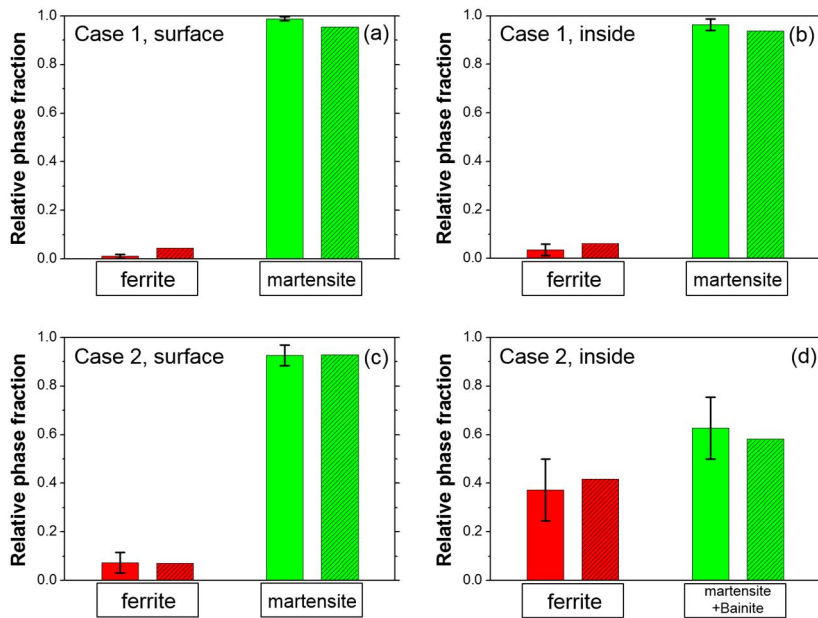


Figure 10.

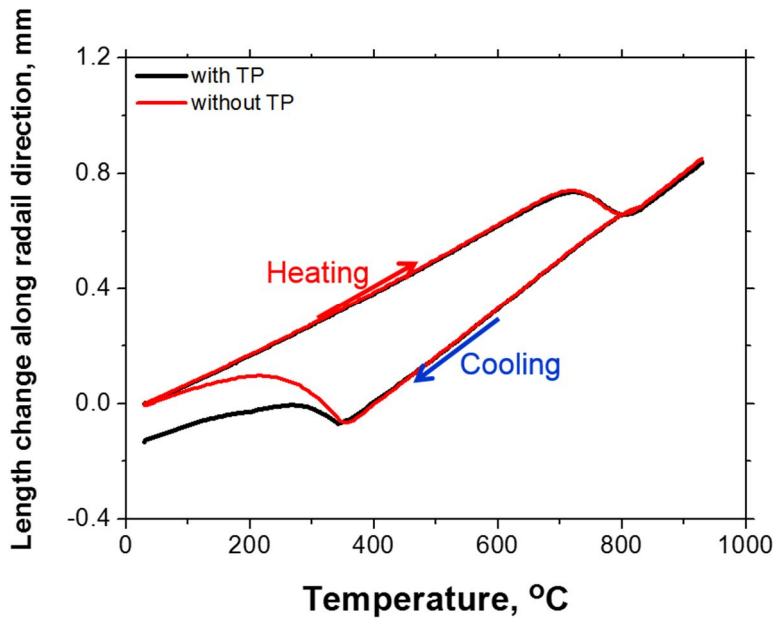


Figure 11.

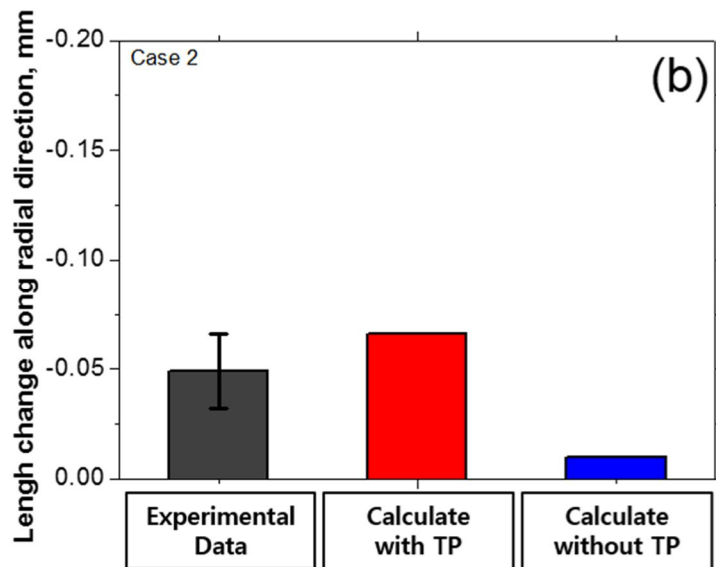
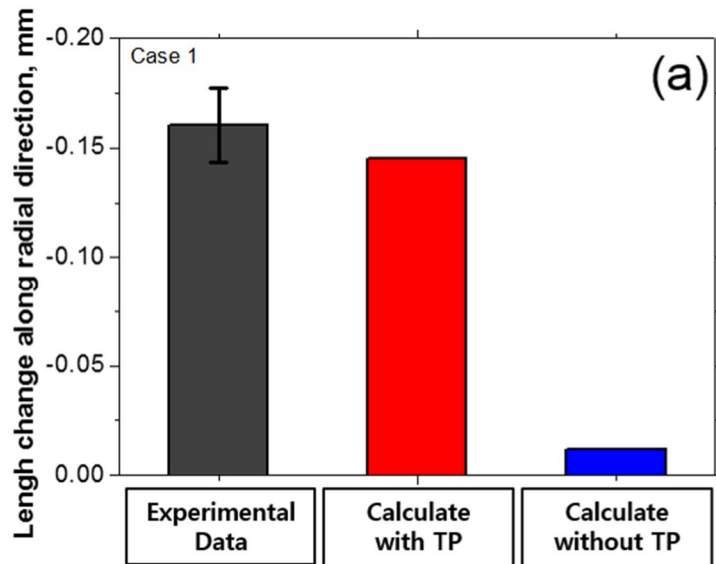


Figure 12.

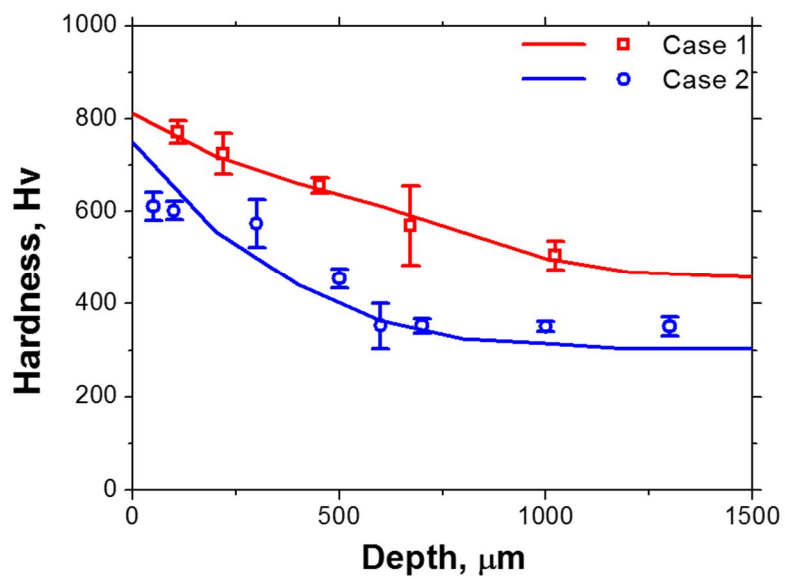


Figure 13.

4.5 Conclusion

A numerical model was developed considering the deformation, temperature history, carbon diffusion, and phase fraction to analyze the thermo-mechanical and metallurgical behavior of annulus gear ring at various carburizing heat treatments. The profiles of carbon concentration of the gear ring were calculated by the finite element simulation based on Fick's law. The kinetics for diffusional and displacive phase transformations was modeled by incorporating the carbon concentration inside the gear. The total deformation due to the phase transformation, transformation plasticity, and thermal expansion/contraction was implemented into the finite element code. The developed model considering the transformation plasticity accurately predicted the length change in comparison to the measured data. This result indicates that the transformation plasticity plays an important role in unexpected dimensional instability in industrial applications. From this model, the effect of carburizing heat treatment conditions on the phase fraction and hardness distribution in the gear were simulated and compared to the experimental data.

4.6 References

- [1] I. Lee, Plasma nitrocarburizing techniques with quenching and tempering for manufacture of vehicle parts, *Korean J. Met. Mater.* 53 (2015) 398-405.
- [2] R. Gorockiewicz, The kinetics of low-pressure carburizing of alloy steels, *Vacuum* 86 (2011) 448-451.
- [3] R.L. Liu, Y.J. Qiao, M.F. Yan, Y.D. Fu, Layer growth kinetics and wear resistance of martensitic precipitation hardening stainless steel plasma nitrocarburized at 460 °C with rare earth addition, *Met. Mater. Int.* 19 (2013) 1151-1157.
- [4] Z. Li, R.V. Grandhi, R. Shivpuri, Optimum design of the heat-transfer coefficient during gas quenching using the response surface method, *Int. J. Mach. Tool Manu.* 42 (2002) 549-558.
- [5] D. Coupard, T. Palin-luc, P. Bristiel, V. Ji, C. Dumas, Residual stresses in surface induction hardening of steels: comparison between experiment and simulation, *Mater. Sci. Eng. A* 487 (2008) 328-339.
- [6] P. Kula, R. Pietrasik, K. Dybowski, Vacuum carburizing—process optimization, *J. Mater. Process. Technol.* 164-165 (2005) 876-881.
- [7] G.-S. Song, X.-H. Liu, G.-D. Wang, X.-Q. Xu, Numerical simulation on carburizing and quenching of gear ring, *J. Iron Steel Res. Int.* 14 (2007) 47-52.
- [8] H. Altena, F. Schrank, Low pressure carburizing with high pressure gas

quenching, VDI. Bericht. 21 (2002) 27-32.

[9] T. Inoue, K. Arimoto, Development and implementation of CAE System “HEARTS” for heat treatment simulation based on metallo-thermo-mechanics, J. Mater. Eng. Perform. 6 (1997) 51-60.

[10] D.Y. Ju, W.M. Zhang, Y. Zhang, Modeling and experimental verification of martensitic transformation, Mater. Sci. Eng. A 438 (2006) 246-250.

[11] Y. Sun Response of cast austenitic stainless steel to low temperature plasma carburizing, Mater. Des. 30 (2009) 1377–1380.

[12] O. Asi, A.C. Can, J. Pineault, M. Belassel, The effect of high temperature gas carburizing on bending fatigue strength of SAE 8620 steel, Mater. Des. 30 (2009) 1792-1797.

[13] H.N. Han, J.K. Lee, A constitutive model for transformation superplasticity under external stress during phase transformation of steels, ISIJ Int. 42 (2002) 200-205.

[14] H.-H. Cho, Y.-G. Cho, Y.-R. Im, J.K. Lee, J.-H. Kwak, H.N. Han, A finite element analysis for asymmetric contraction after coiling of hot-rolled steel, J. Mater. Process. Technol. 210 (2010) 907-913.

[15] G.W. Greenwood, R.H. Johnson, The deformation of metals under small stresses during phase transformations, Proc. R. Soc. A. (London) 83 (1965) 403.

[16] H.N. Han, C.G. Lee, C.-S. Oh, T.-H. Lee, S.-J. Kim, A model for deformation behavior and mechanically induced martensitic transformation of

- metastable austenitic steel, *Acta Mater.* 52 (2004) 5203-5214.
- [17] M.-G. Lee, S.-J. Kim, H.N. Han, Crystal plasticity finite element modeling of mechanically induced martensitic transformation (MIMT) in metastable austenite, *Int. J. Plast.* 26 (2010) 688-710.
- [18] H.N. Han, J.K. Lee, D.-W. Suh, S.-J. Kim, Diffusion-controlled transformation plasticity of steel under externally applied stress, *Philos. Mag.* 87 (2007) 159-176.
- [19] Y. Desalos, Comportement dilatométrique et mécanique de l'Austénite Métastable d'un Acier A 533, IRSID Report n. 34 (1981) 44.
- [20] P. Zwigl, D.C. Dunand, A numerical model of transformation superplasticity for iron, *Mater. Sci. Eng. A* 262 (1999) 166-172.
- [21] H.N. Han, D.-W. Suh, A model for transformation plasticity during bainite transformation of steel under external stress, *Acta Mater.* 51 (2003) 4907-4917.
- [22] H.N. Han, C.-S. Oh, G. Kim, O. Kwon, Design method for TRIP-aided multiphase steel based on a microstructure-based modelling for transformation-induced plasticity and mechanically induced martensitic transformation, *Mater. Sci. Eng. A* 499 (2009) 462-468.
- [23] H.-J. Jeong, M.-J. Kim, D.-W. Kim, D.-W. Suh, J.-K. Oh, H.N. Han, Transformation plasticity in boron-bearing low carbon steel, *Met. Mater. Int.* 21 (2015) 799-804.
- [24] A. Sugianto, Numerical simulation and experimental verification of

carburizing-quenching process of SCr420H steel helical gear, *J. Mater. Process. Technol.* 209 (2009) 3597-3609.

[25] H.N. Han, J.K. Lee, H.J. Kim, Y.-S. Jin, A model for deformation, temperature and phase transformation behavior of steels on run-out table in hot strip mill, *J. Mater. Process. Technol.* 128 (2002) 216-225.

[26] Y.-G. Cho, Y.-R. Im, J.K. Lee, D.-W. Suh, S.-J. Kim, H.N. Han, A finite element modeling for dilatometric nonisotropy in steel, *Mater. Sci. Eng. A* 42A (2011) 2094-2106.

[27] D.-W. Kim, Y.-G. Cho, H.-H. Cho, S.H. Kim, W.B. Lee, M.-G. Lee, H.N. Han, A numerical model for vacuum carburizing of an automotive gear ring, *Met. Mater. Int.* 6 (2011) 885-890.

[28] M. Jung, Y.-K. Lee, A predictive model for carbon concentration profile of vacuum carburized steels with acetylene, *Met. Mater. Int.* 15 (2009) 971-975.

[29] W.A. Johnson, R.F. Mehl, *Trans. AIME.* 135 (1937) 416.

[30] M. Avrami, Kinetics of Phase Change. I General Theory, *J. Chem. Phys.* 7 (1939) 1103-1112.

[31] A.N. Kolmogorov, I.G. Petrovskii, N.S. Piskunov, A study of the equation of diffusion with increase in the quantity of matter, and its application to a biological problem, *Bjul. Moskovskogo Gos. Univ.* 1(7) (1937) 1-26.

[32] D.P. Koistinen, R.E. Marburger, A general equation prescribing the extent of the austenite-martensite transformation in pure iron-carbon alloys and plain

- carbon steels, *Acta Metall. Mater.* 7 (1959) 447.
- [33] E. Sheil, *Archiv fuer Eisenhuettenwesen* 8 (1935) 565.
- [34] H.N. Han, S.-H. Park, Model for cooling and phase transformation behavior of transformation induced plasticity steel on runout table in hot strip mill, *Mater. Sci. Technol.* 17 (2001) 721-726.
- [35] J.O. Andersson, T. Helander, L. Höglund, F. Shi, B. Sundman, ThermoCalc and DICTRA, computational tools for materials science, *CALPHAD.* 26 (2002) 273.
- [36] B. Sundman, B. Jansson, J.O. Andersson, *CALPHAD.* 9 (1985) 153–190.
- [37] Z. Zhao, C. Liu, Y. Liu, D.O. Northwood, A new empirical formula for the bainite upper temperature limit of Steel, *J. Mater. Sci.* 36 (2001) 5045-5056.
- [38] J. Årgen, A revised expression for the diffusivity of carbon in binary Fe–C austenite, *Scripta Metall.* 20 (1986) 1507–1510.
- [39] R.A. Grange, H.M. Stewart, The temperature range of martensite formation, *Trans. AIME.* 167 (1946) 467-501.
- [40] ABAQUS Inc., User's manuals v6.10, 2010.
- [41] H.J. Frost, M.F. Ashby, *Deformation Mechanism Maps, The Plasticity and Creep of Metals and Ceramics.* Pergamon Press, 1982, pp. 21.
- [42] J. Mieltien, *Solidification-related thermo-physical data for low-alloyed and stainless steels.* Helsinki University of Technology, 1995.
- [43] S. Koric, B.G. Thomas, *Thermo-mechanical models of steel*

solidification based on two elastic visco-plastic constitutive laws, *J. Mater. Process. Technol.* 197 (2008) 408–418.

[44] S. Nanba, M. Katsumata, T. Inoue, S. Nakajima, G. Anan, A. Hiramatsu, A. Moriya, T. Watanabe, M. Umemoto, *CAMP-ISIJ.* 3 (1990) 871.

[45] M.-G. Lee, S.-J. Kim, Elastic-plastic constitutive model for accurate springback prediction in hot press sheet forming, *Met. Mater. Int.* 18 (2012) 425-432.

[46] Y. Misaka, Formulatization of mean resistance to deformation of plain C steels at elevated temperature, *JSJP.* 8 (1967) 414-422.

[47] J.Y. Kang, D.H. Kim, S.-I. Balk, T.-H. Ahn, Y.-W. Kim, H.N. Han, K.H. Oh, H.-C. Lee, S.H. Han, Phase analysis of steels by grain-averaged EBSD functions, *ISIJ Int.* 51 (2011) 130-136.

[48] J.Y. Kang, S.J. Park, D.-W. Suh, H.N. Han, Estimation of phase fraction in dual phase steel using microscopic characterizations and dilatometric analysis, *Mater. Charact.* 84 (2013) 205-215.

[49] J.C. Ion, L.M. Anisdahl, A PC-based system for procedure development in laser transformation hardening, *J. Mater. Process. Technol.* 65 (1997) 261-267.

[50] J.H. Hollomon, L.D. Jaffe, *Trans. AIME.* 162 (1945) 223-249.

Chapter 6

Total conclusions

Phase transformation behaviors play an important role to improve material properties of the steels. Therefore it is necessary to predict accurate phase transformation behaviors using appropriate model. However, classical phase transformation model is mostly based on only the effect of alloying element and temperature, thus it has a certain limitation to consider the complex AHHS including retained austenite, precipitation, and carburizing. In this paper, there are various attempts in order to overcome those limitations

Firstly, this paper studied the method of dilatometric analysis to analyze the phase transformation behaviors of AHHS with retained austenite. Developed dilatometric analysis method is based on lattice parameter and atomic volume of each phase and additionally consider transformation plasticity and enrich of alloying element. Using the thermodynamic data and equations embedded in the method, it can distinguish the type of BCC structure. Analysis of two specimens which has different Mn, the strong austenite stabilizer, we can verify the accuracy of developed method and find various parameters concerning transformation plasticity and fraction of retained austenite. This method is preferred to obtain the fraction of final fraction of retained austenite very simply and phase transformation kinetics of

retained austenite steel.

Secondly, in this study, the precipitation behaviors of Nb in the austenite region are measured by TEM observation. The precipitation behaviors are accelerated with addition of Si and the fastest at 865 °C. Using the precipitation model based on KWN and GBB model, we predict various precipitation behaviors and determine appropriate interfacial energy between matrix and precipitate using size correction expression. Phase transformation model combined with Nb precipitation kinetics is modeled based on Johnson–Mehl–Avrami–Kolmogorov equation modified to reflect Nb solid solution and precipitation. Using this modified model and dilatometric analysis, effect of precipitated Nb which accelerates phase transformation is determined.

Lastly, a numerical model was developed considering the deformation, temperature history, carbon diffusion, and phase fraction to analyze the thermo-mechanical and metallurgical behavior of annulus gear ring at various carburizing heat treatments. The profiles of carbon concentration of the gear ring were calculated by the finite element simulation based on Fick's law. The kinetics for diffusional and displacive phase transformations was modeled by incorporating the carbon concentration inside the gear. The total deformation due to the phase transformation, transformation plasticity, and thermal expansion/contraction was implemented into the finite element code. The developed model considering the transformation plasticity accurately predicted the length change in comparison to the measured data. This result

indicates that the transformation plasticity plays an important role in unexpected dimensional instability in industrial applications. From this model, the effect of carburizing heat treatment conditions on the phase fraction and hardness distribution in the gear were simulated and compared to the experimental data.

국문 초록

철강 소재에서의 최근의 이슈는 더욱 뛰어난 물성을 가지면서도 가벼운 새로운 철강을 개발하는 것이고, 이러한 기술은 자동차 소재 등에서 널리 이용되고 있다. Advanced high strength steel (AHSS)는 이러한 특성을 만족시키는 뛰어난 철강 소재로 다년간의 연구가 진행되어 왔다. 초기의 AHSS는 Transformation induced plasticity steel (TRIP)와 Dualphase steel (DP) 등으로 대표되며, 모두 이전의 전통적인 철강 소재에 비해 뛰어난 강도를 갖는다. 이후의 단계인 Ultra - Advanced high strength steel (U-AHSS) 소재는 Twinning induced plasticity steel (TWIP) 등으로 대표되며, 매우 뛰어난 강도와 연성을 가지지만, 망간 등의 합금 원소가 대량 첨가되어, 가격이 비싸고, 제조 공정상의 어려움이 나타난다. 그러므로 최근에는 AHSS와 U-AHSS의 중간 정도의 물성을 가지면서, 가격이나 공정 과정에서의 단점을 보완한 Extra - Advanced high strength steel (X-AHSS)의 개발에 많은 노력을 기울이고 있다.

이러한 X-AHSS 소재의 개발을 위해서는 이전 철강 소재보다 매우 복잡한 열처리나 합금 원소 첨가가 요구되며, 이러한 과정을

통하여, 철강의 상변태를 조절하는 것이 기술 개발의 핵심이다. 이러한 기술 개발에 있어서 X-AHSS 소재의 상변태를 정확히 예측하는 모델을 개발하는 것은 공정 최적화 및 신강종 설계에 필수적이지만, 기존의 고전적 상변태 모델은 철강의 상변태를 단순히 온도와 조성의 함수로만 가정하여, X-AHSS와 같은 복잡한 강종의 상변태 예측에는 적합하지 않다. 그러므로 이번 연구에서는 잔류 오스테나이트, 석출, 침탄 등과 같은 복잡한 현상을 고려할 수 있는 상변태 모델을 만들고 이를 적용하는 연구를 수행 하였다.

먼저, 격자 상수와 변태 소성을 기반으로 하여, 잔류 오스테나이트를 포함하는 AHSS의 상변태를 예측하는 방법을 연구 하였다. 이러한 연구 방법은 기존의 지렛대 법칙을 이용한 상변태 분석법과는 달리 잔류 오스테나이트가 남거나, 부분적인 열처리를 거친 시편의 상변태를 정확히 분석할 수 있고, 내부에 포함된 열역학 데이터를 이용하여, 생성된 상의 종류를 구별하는 기능 또한 포함하고 있다. 이러한 방법을 이용하여, 강력한 오스테나이트 안정제인 망간의 함유량이 다른 다양한 시편을 분석하여, 개발된 모델이 잔류 오스테나이트 상의 상변태를 정확히 예측하는 것을 확인 하였다.

두번째로, 철강 소재의 석출을 고려한 상변태 모델을 개발하였다.

일반적으로 니오븀과 같이 석출물을 잘 생성하는 합금 원소의 경우, 철강 내에 용해되어 있을 때는 철강의 상변태를 지연 시키지만, 철강 내에 석출 되어 있을 경우는 핵생성의 시작점이 되거나, 결정립 성장을 억제시켜 상변태를 촉진시키는 역할을 한다. 이번 연구에서는 투과전자현미경과 상용 석출 계산 프로그램인 matcalc를 활용하여 철강 소재의 석출 거동을 분석하고 이를 고려하여 상변태 모델을 제작하였으며, 석출량을 조절한 다양한 열처리를 통하여 제작된 모델의 정확성을 검증하였다.

마지막으로 침탄 현상을 고려한 상변태 모델을 제작하고, 이를 실제 공정에 적용시켜 해석하는 연구를 진행하였다. 침탄 열처리를 진행하게 되면, 철강 소재 내의 탄소 농도가 위치 별로 달라지게 되며, 이로 인해 위치별 상변태 거동이 달라지게 된다. 그러므로 탄소 농도의 변화에 따른 상변태를 고려할 수 있는 상변태 모델을 제작하고, 이를 이용하여 실제 공정에서 발생하는 침탄 열처리 과정을 유한요소해석을 통해 해석하였다. 그 결과 탄소 농도 변화, 미세조직 변화 등을 관찰 할 수 있었으며, 변태 소성 등의 변화에 따른 열변형 현상 또한 정확히 예측할 수 있었다.

본 연구를 통해, X-AHSS와 같은 복잡한 공정을 이용한 철강 소재의 열처리를 정확히 예측하는 상변태 모델을 개발하고, 그

정확성을 검증 하였다. 개발된 모델과 제안된 방법은 철강의 새로운 철강 소재의 개발과 공정 최적화에 크게 기여 할 수 있을 것이라 기대된다.

핵심어: 상변태, 오스테나이트, 격자 상수, 변태 소성, 탄소 농축, 석출, 탄소 확산, 침탄 열처리, 유한요소해석, 침탄 해석, 열-변형 해석, 경도

Student number: 2010-20577